

# JGR Solid Earth

## RESEARCH ARTICLE

10.1029/2021JB023317

### Key Points:

- We develop a full time-series inversion (FTI) algorithm to obtain fault afterslip models using various geodetic time series observations
- We apply the FTI algorithm to invert SAR time series for the 2017 Sarpol-e Zahab earthquake afterslip processes
- Different decay times and frictional behaviors are resolved for afterslip in the up- and downdip portions of the coseismic slip of the Sarpol-e Zahab earthquake

### Supporting Information:

Supporting Information may be found in the online version of this article.

### Correspondence to:

H. Yue,  
[yue.han@pku.edu.cn](mailto:yue.han@pku.edu.cn)

### Citation:

Yue, H., Wang, K., Xue, L., Shen, Z., & Sun, J. (2022). Postseismic process inversion using full time series of surface deformation: Full time-series inversion (FTI) theory and its application to the 2017 Sarpol-e Zahab earthquake. *Journal of Geophysical Research: Solid Earth*, 127, e2021JB023317. <https://doi.org/10.1029/2021JB023317>

Received 27 SEP 2021

Accepted 2 SEP 2022

### Author Contributions:

**Conceptualization:** Han Yue, Lian Xue  
**Data curation:** Kang Wang  
**Formal analysis:** Han Yue, Kang Wang  
**Investigation:** Kang Wang  
**Methodology:** Han Yue, Lian Xue, Zhengkang Shen, Jianbao Sun  
**Software:** Han Yue  
**Validation:** Han Yue  
**Visualization:** Han Yue  
**Writing – original draft:** Han Yue  
**Writing – review & editing:** Han Yue, Kang Wang, Lian Xue, Zhengkang Shen, Jianbao Sun

## Postseismic Process Inversion Using Full Time Series of Surface Deformation: Full Time-Series Inversion (FTI) Theory and Its Application to the 2017 Sarpol-e Zahab Earthquake

Han Yue<sup>1,2,3</sup> , Kang Wang<sup>4</sup> , Lian Xue<sup>1,3</sup>, Zhengkang Shen<sup>1,5</sup>, and Jianbao Sun<sup>6</sup> 

<sup>1</sup>School of Earth and Space Sciences, Peking University, Beijing, China, <sup>2</sup>Center for Habitable Intelligent Geosciences, Institute of Artificial Intelligence, Peking University, Beijing, China, <sup>3</sup>Hongshan Geophysical National Observation and Research Station, Peking University, Beijing, China, <sup>4</sup>Department of Earth and Planetary Science, University of California, Berkeley, Berkeley, CA, USA, <sup>5</sup>Department of Earth, Planetary, and Space Sciences, University of California, Los Angeles, Los Angeles, CA, USA, <sup>6</sup>State Key Laboratory of Earthquake Dynamics, Institute of Geology China Earthquake Administration, Beijing, China

**Abstract** Postseismic processes provide important opportunities to probe into and investigate the frictional, viscous, and porous properties of the seismogenic fault and the surrounding Earth media. To accommodate the temporal and spatial resolutions and long-term baseline stability of different deformation data, we develop a full time-series inversion (FTI) technique, which jointly inverts for afterslip patterns using full time series of Global Navigation Satellite System, SAR, and strainmeter data. The FTI linearizes the inversion problem with a prescribed source evolution function to achieve efficient inversion. We conduct synthetic tests to validate the spatial and temporal resolution of the FTI algorithm. FTI outperforms static inversion techniques in terms of inversion stability under high noise level. We apply different parameterization strategies to evaluate its resolution for slip evolution parameters. The tests show that FTI can discriminate spatially separated afterslip with distinct evolution functions. Finally, we apply FTI to investigate the afterslip process following the 2017  $M_w$  7.3 Sarpol-e Zahab earthquake that occurred along the Iran-Iraq border in northwestern Zagros using Synthetic Aperture Radar Interferometry time series derived from the Sentinel-1 observations 1 year after the mainshock. Similar to the synthetic tests, the algorithm is capable to discriminate afterslip with different evolution functions in the up- and downdip portions of the coseismic rupture zone. By comparing with the stress-driven afterslip model simulated using rate-strengthening frictional law, we demonstrate the stability of FTI in resolving the afterslip process. We emphasize the importance of incorporating early postseismic observations for deciphering afterslip evolution and frictional parameters.

**Plain Language Summary** Postseismic processes provide important opportunities to probe into and investigate the in-elastic properties of the earth medium. Observations obtained using different means such as Global Navigation Satellite System, SAR, and strainmeter can be utilized to realize such purposes, and each of them has unique merit to provide potentially high spatial resolution, high temporal resolution, and/or stable baselines. We develop an algorithm that can use these three different observations together in a joint inversion work. This algorithm, namely, full time-series inversion (FTI), can flexibly incorporate variations of afterslip parameters in a joint inversion to investigate different frictional properties of the fault plane. We particularly adopt the FTI algorithm to study the afterslip pattern of the 2017 Sarpol-e Zahab earthquake, and find that its afterslips in the up- and downdip portions have different characteristic decay times. This conclusion draws physical significance which is different from some previous works.

## 1. Introduction

Earthquakes produce stress loading to the earth media, which initiates responses at different temporal and spatial scales related to various media properties. Short period (within hours) responses, for example, elastic wave propagation and coseismic deformation, generally reflect elastic responses of the earth media, which is the major research topic of seismology. Long-term (from days to years) responses, known as postseismic deformation, are important topics of geodetic investigations. Such studies focus on non-elastic media properties that control long-term processes, for example, earthquake cycle, tectonic, and geodynamic processes. Proposed mechanisms of postseismic deformation include afterslip on the fault plane (Scholz, 1998), viscous relaxation in the lower

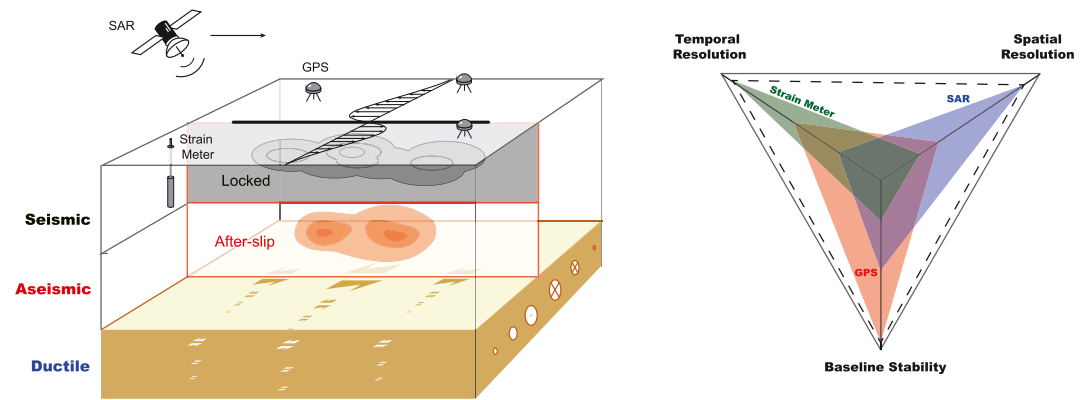


**Figure 1.** Illustrative cartoons depicting postseismic relaxation processes and characteristics of surface deformation observation techniques. The left-panel plots coseismic and afterslip patterns as gray and red-filled patches in the up- and down-dip fault portions, respectively. Viscoelastic relaxation in the lower crust is indicated as arrow pairs. Postseismic deformation at the surface is observed by Synthetic Aperture Radar Interferometry, GPS, and strainmeters. The right panel describes the resolution in the spatial, temporal, and baseline domains of each data type.

crust and/or upper mantle (Pollitz et al., 2006), pore-elastic rebound at shallow depths (Jonsson et al., 2003), and fault-zone collapse (for example, Fielding et al., 2009). Observations of postseismic deformation, therefore, provide important information on various mechanical properties of the earth media, such as frictional properties of faults in the case of afterslip, the effective viscosity of the Earth's lithosphere in the case of viscoelastic relaxation, hydrological properties of the porous layer in the case of a poroelastic rebound, and fault zone damage related to its recovery in the case of fault-zone collapse. Particularly, afterslip plays an important role in accommodating the strain release during an earthquake cycle, so accurately characterizing the spatial and temporal evolution of afterslip following a large earthquake is critical to assessing the time-dependent seismic hazard risk (e.g., Bedford et al., 2013; Fukuda & Johnson, 2021; Hu et al., 2016; Wei et al., 2015; Yue et al., 2021; Yue et al., 2020).

Postseismic processes typically drive the ground surface to deform at low velocities ( $<1$  cm/day, e.g., Hsu et al., 2011), thus it requires the instruments/techniques to have a good response at low-frequency bands to capture such processes. Among various geophysical observations, Global Navigation Satellite Systems (GNSS), Synthetic Aperture Radar Interferometry (InSAR), and strainmeters are most commonly used to investigate the postseismic processes (Figure 1). The merits and limitations of each kind of data are briefly summarized as follows. GNSS stations can continuously receive signals from satellites providing continuous monitoring of 3-D displacements at the stations. Modern high-rate GNSS (hr-GNSS) instruments can have a sampling frequency of several tens of hertz, which is valuable to monitor the dynamics of early postseismic deformation (e.g., Twardzik et al., 2021), while its uncertainties increase with sampling rates (e.g., Larson et al., 2007). Thus, averaging the position solutions over a period of time (e.g., a day) is generally required to achieve millimeter precision and resolve subtle postseismic deformation. The most commonly used GNSS data in postseismic studies are daily time series. Depending on the reference framework used, GNSS survey can provide the absolute measurement of surface displacement with good baseline stability. Here, baseline stability refers to the ability of an instrument to precisely measure relative values of samples separated by long spatial or temporal scales (King & Williams, 2009). Particularly in this study, we focus on the temporal baseline, which evaluates if the overall displacement of time series can be precisely recovered over a long term. In general, differential-based measurement data have a shortcoming of unstable temporal baseline. Integrating differential displacements or velocities accumulates errors of each time sample, thus cannot precisely recover long-term displacement. In seismological research, such a limitation persists when using velocity or acceleration waveforms to recover ground displacements. Because GNSS measurements are referred to the earth coordinate, which is a stable framework over large spatial and temporal scales (King & Williams, 2009), GNSS data are commonly used to correct for spatial and temporal shifts of other data (e.g., R. Wang et al., 2011). Thus, baseline stability is significant merit of GNSS data.

SAR satellites periodically scan the target region at high spatial resolution (tens to hundreds of meters), while its temporal resolution is limited by the satellite revisiting intervals. Among the currently available civilian SAR systems, Sentinel-1, including two satellites Sentinel-1A and 1B, have the shortest revisiting interval of 6 days,

when both satellites are in full operation. Consisting of multiple X-band satellites, the COSMO-SkyMed (CSK) system can have a revisit time as short as 1 day. However, data from the CSK system are generally not free of charge, limiting its wide application in the science community. Interferometry of two SAR images (InSAR) provides relative displacements between epochs of image acquisitions (e.g., Bürgmann et al., 2000; Massonnet et al., 1993). Because phase correlation generally decreases with the temporal intervals of images for interferometry, relative displacements can only be made for images collected within a relatively short period (generally within months), and its temporal correlation varies significantly with vegetation and climate conditions (e.g., Hagberg et al., 1995). Long-term InSAR time series can be constructed from interferograms of short temporal baseline series (e.g., Berardino et al., 2002), while this technique also suffers from losing relative displacement precision in long terms (long-term baseline), when the time series duration is much longer than the average temporal baselines of the interferograms, which limits its long term baseline stability. Therefore, SAR time series commonly rely on GNSS data to correct its displacement drifts (Janssen et al., 2004; Li, 2005).

Strainmeters measure ground deformation (strains) at hundreds of meter depth in bore-hole stations. The accuracy of strainmeters can achieve micro-strain precision ( $10^{-6}$ ) at high sampling rates, for example, 1 Hz for PBO stations, which is sensitive to both emergent and slow processes including afterslips, aftershocks, and solid earth tides. Because the spatial variation of strain fields is at a higher gradient than the displacement fields, afterslip-related strain signals are more prominent in near-fault stations (Yue et al., 2021). In addition, strainmeters are sensitive to the site environment including temperature, atmospheric pressure, and instrument stability, which commonly have long-term drifts (Agnew, 1986; Jeffery & Sydenham, 1973). Therefore, strainmeters are more suitable to evaluate short-term (within several days) postseismic deformation.

The merit and limitations of the three major data sets are summarized in Figure 1b. It clearly shows that the spatial resolution, temporal resolution, and baseline stability of the three data sets compensate for each other. It is intuitive to adopt different data sets in a joint inversion to resolve processes with both high spatial and temporal resolutions. Such a joint inversion approach using coseismic observations (e.g., Yue et al., 2020), has been successfully adopted in earthquake rupture process inversions. For after-slip inversion, traditional methods using geodetic observations cut the time series into segments and invert for corresponding slip models during each temporal segment either jointly or separately. For example, GNSS data are used to investigate afterslip of megathrust events including the 2005 Nias earthquake (Hsu et al., 2006), 2010 Maule earthquake (Bedford et al., 2013; Lin et al., 2013), and 2011 Tohoku earthquake (Fukuda & Johnson, 2021). InSAR data are more commonly used to obtain afterslip models of continental earthquakes, for example, the 1999 Izmit earthquake (Cakir et al., 2003) and the 2010 south Napa earthquake (Floyd et al., 2016; Wei et al., 2015). Because surface deformation produced by point dislocation (which forms the basis of Green's function for deformation) can be theoretically computed, it is relatively easy to realize linear inversion for afterslip, while investigating the viscous properties generally requires numerical simulation (e.g., Diao et al., 2018; Hu et al., 2016; Pollitz et al., 2006; Wang & Fialko, 2018]. Other methods, including Principal Component Analysis (PCA) or Independent Component Analysis (ICA), Network Inversion Filter (NIF), and Network Strain Filters (NSF), make use of full GNSS time series and can obtain an overall evolution function of transient fault slip. The PCA method explores the spatial and temporal evolution of postseismic transients and decomposes the geodetic time series into principal components. Inversion is performed on each spatial component to resolve afterslip associated with the respective temporal functions (Kositsky & Avouac, 2010). This method is successfully adopted to investigate the afterslip pattern of the 2015 Gorkha earthquake (Gualandi, Avouac, et al., 2017) and the 2014 Papamoa earthquake (Gualandi, Perfettini, et al., 2017). The NIF method associates the spatial deformation pattern of a GNSS network to that caused by fault slip and uses the Kalman filter to determine its temporal evolution function (Segall and Matthews, 1977). NSF uses a similar strategy as NIF, yet it does not associate deformation with fault slip (Ohtani et al., 2010), but only extracts the spatial correlation features. The focus of NIF and NSF is to provide continuous monitoring of transient deformation events using GNSS network data, which explores data spatial coherency to find local deformation anomalies.

Joint inversion incorporating three types of data is rare in previous studies. Despite the sparsity of strainmeters, the distinct temporal sampling of InSAR and GNSS data are not well accommodated in the abovementioned methods. Yue et al. (2021) developed a FTI algorithm, which jointly adopts full time series of GNSS, InSAR, and strainmeter observations in a linear inversion approach to invert for afterslip following the  $M_w$  6.4 foreshock and the  $M_w$  7.1 mainshock of the 2019 Ridgecrest earthquake sequence. The key assumption of FTI is to assume an analytical form of evolution function for the underlying postseismic relaxation mechanism (e.g., a logarithmic

function in the case of afterslip), which enables analytical calculation of temporal Green's functions to perform a linear inversion. The design of FTI is particularly intended for modeling the postseismic processes, which often have a clear initiation time and well established mathematical representations for the underlying relaxation mechanisms. Thus, it is relatively straightforward to assume a temporal evolution function referenced to physical models. This approach is different from some of the data-driven methods, for example, PCA and ICA, which aim to find a set of spatially and temporally independent functions that can best explain the data variance through a series of the matrix transformation. PCA and ICA are powerful methods in extracting the prominent features of a postseismic deformation process, but it is sometimes difficult to find clear physical interpretations for the corresponding "components." NIF adopts a hybrid approach. For instance, when characterizing the deformation related to afterslip, NIF inverts for the distribution of afterslip at each time epoch to characterize its spatial pattern and uses a Kalman filter to estimate the temporal evolution function. Similar to PCA and ICA, the resulting temporal evolution function from a NIF inversion may also strongly depend on the data quality that can make the interpretation of underlying source dynamics less straightforward.

FTI, on the other hand, assumes a certain type of evolution function for a given postseismic relaxation mechanism, which is arguably more applicable to postseismic process inversions, given that the measurements of postseismic deformation often have relatively low signal-to-noise ratio (SNR) and are spatially sparse. The FTI method was particularly designed for the unique observations of the 2019 Ridgecrest earthquake sequence in southern California, which included the high temporal resolution of strainmeter data, the high spatial resolution of InSAR time series and a stable baseline of GNSS solutions to resolve afterslip patterns for that sequence. However, Yue et al. (2021) lacked a thorough discussion of the inversion theory and its performance in resolving more complex postseismic deformation processes, for example, an afterslip model that contains two distinct relaxation times. As a complement to Yue et al. (2021), in this paper, we discuss comprehensively the assumptions, discretization, and correction methods of FTI. Synthetic tests are conducted to evaluate its performance under different assumptions.

### 1.1. The 2017 $M_w$ 7.3 Sarpol-e Zahab (Iran) Earthquake

As described above, the basic concept and algorithm of the FTI were introduced by Yue et al. (2021). Yet, one remaining question is whether the FTI can discriminate afterslip processes with different decaying characteristics. For the Ridgecrest earthquake, the FTI of GNSS and strainmeter observations suggested afterslip of different decaying times, but it is difficult to determine if such phenomena originated from a realistic physical process or different data resolution, since duration of credible strainmeter data is close to the sample interval of the GNSS data (Yue et al., 2021). Therefore, it is necessary to test the FTI performance in a case study where available data sets can well resolve the spatial and temporal variation of afterslip. An ideal case would be that the geometry of the coseismic rupture is relatively simple, and that the postseismic deformation from different relaxation mechanisms can be easily separated, whereas the postseismic surface deformation exhibits clear spatial and temporal variations. The 2017  $M_w$  7.3 Sarpol-e Zahab (Iran-Iraq) earthquake appears to be such a case. The Sarpol-e Zahab earthquake occurred on 12 November 2017 at 18:18 UTC, along the border between Iran and Iraq, causing nearly 600 deaths and widespread damages. This event is a thrust-dextral event that occurred along the Main Frontal Thrust, a topographic and structural relief step that divides the Zagros mountain range from its foreland to the southwest (Figure 3).

The coseismic rupture characteristics of the 2017 Sarpol-e Zahab earthquake were extensively studied (e.g., Liu & Xu, 2019; Vajedian et al., 2018; Wang & Bürgmann, 2020). These studies all reveal a unilateral rupture along the strike directly to the SSW direction. Afterslip of the 2017 Sarpol-e Zahab earthquake, including its spatial distribution and temporal evolution, has also been investigated by different groups, (e.g., Liu & Xu, 2019; Wang and Bürgmann, 2020). Wang and Bürgmann (2020) use a Bayesian inversion scheme to investigate the geometry of the coseismic rupture and subsequent afterslip. They find that the afterslip updip of the coseismic rupture occurred along a shallow angle ( $5^\circ$ ) detachment that possibly corresponds to a mechanically weak zone within the sedimentary cover. They use both kinematic inversion and numerical simulation methods to investigate the spatial and temporal distribution of afterslip. It is shown that during the InSAR observation period (2017–2018), the inferred afterslip updip of the coseismic rupture was much larger than that of the downdip region, although the coseismic stress loadings on both portions are comparable. Liu and Xu (2019) focus on the updip afterslip pattern and use a logarithmic function to fit its evolution function. Further conclusions regarding frictional parameters, for example,  $a$ - $b$  values, are drawn by Liu and Xu (2019). The strategy of afterslip inversion in Liu and Xu (2019)

is similar to FTI, although they emphasize more on its ability to correct for early afterslip in coseismic rupture inversion.

In this study, we apply FTI to the postseismic InSAR time series of the Sarpol-e Zahab earthquake to evaluate its performance in discriminating distinct afterslip processes. We show that FTI is capable of discriminating distinct evolution patterns in the up- and down-dip portions of the fault plane, despite that only InSAR data are available for the 2017 Sarpol-e Zahab earthquake. However, we admit that different types of data sets are probably needed to better understand the performance of FTI when it is used to investigate the postseismic deformation of multiple relaxation mechanisms with complex rupture geometries.

## 2. Theory and Method

### 2.1. Quasi-Static and Steady-State Assumption and Model Discretization

In an elastic medium, the full response to a point force load is described by a wave equation

$$C \nabla^2 \mathbf{u}(\mathbf{x}, t) + \rho \ddot{\mathbf{u}}(\mathbf{x}, t) = \mathbf{f}(\mathbf{x}', t) \quad (1)$$

where  $u(x, t)$  is the temporal varying displacement field induced by a temporally varying force of  $f(x', t)$  loaded at  $x'$ .  $C$  and  $\rho$  are, respectively, the elastic moduli and density of the medium. If the source  $f(x', t)$  evolves slowly, one can assume that the acceleration of the medium is negligible, namely, quasi-static assumption, so the inertia term (second term on the left side of the equation) can be neglected. The partial differential equation of a slowly evolving source in an elastic medium can be then described by

$$C \nabla^2 \mathbf{u}(\mathbf{x}, t) = \mathbf{f}(\mathbf{x}', t) \quad (2)$$

which is essentially a Poisson's equation with a temporally varying source. One special feature of Equation 2 is that the derivative operation is only with respect to the space, although both  $u$  and  $f$  include temporal variation. This property essentially means that the spatial relationship between  $u$  and  $f$  determined by the Poisson's equation at any time epoch can be simplified as

$$C \nabla^2 \mathbf{u}(\mathbf{x}) = \mathbf{f}(\mathbf{x}') \quad (3)$$

This means that the temporal evolution of displacement field follows the same time function as  $f$  with the scaling relationship determined by Poisson's equation. If  $f$  is a point dislocation (double-couple forces equivalence) or is distributed over a rectangle sub-fault, its associated displacement field  $u$  (Green's functions) can be analytically computed with the source representation theorem (Aki & Richards, 2002) (e.g., Okada solution [Okada, 1985]). Please note we use  $u(x)$  and  $u(x, t)$  to represent static and dynamic ground displacement field, respectively. The displacement field at location  $x$  produced by a source of unit displacement/slip at  $x'$  can be represented as  $G(x, x')$ . Assuming the source evolution function is  $S(t)$ , the displacement evolution function at location  $x$  can be simply calculated by

$$\mathbf{G}(\mathbf{x}, \mathbf{x}', t) = \mathbf{G}(\mathbf{x}, \mathbf{x}') \mathbf{S}(t, \mathbf{x}') \quad (4)$$

where  $G(x, x')$  represents the response of the medium at a point  $x$  due to the load applied at  $x'$ , and  $S(t, x')$  the temporal evolution of the load at  $x'$ , which we name as the characteristic Slip Evolution Function (SEF) of the postseismic relaxations.

For distributed afterslip on a fault plane, the associated ground displacement can be calculated from integration over a 2D fault plane

$$\mathbf{u}(\mathbf{x}, t) = \iint_{x'} \mathbf{G}(\mathbf{x}, \mathbf{x}') \mathbf{S}(t, \mathbf{x}') \mathbf{m}(\mathbf{x}') d\mathbf{x}' \quad (5)$$

where  $m(x')$  represent the spatial distribution of the postseismic source loading (e.g., afterslip). Similar to the finite fault inversion of fault slip during the coseismic phase, the spatial integration represented in Equation 5 can be discretized as a linear summation of point/rectangle sources over the fault plane. The discrete form of Equation 5 is written as

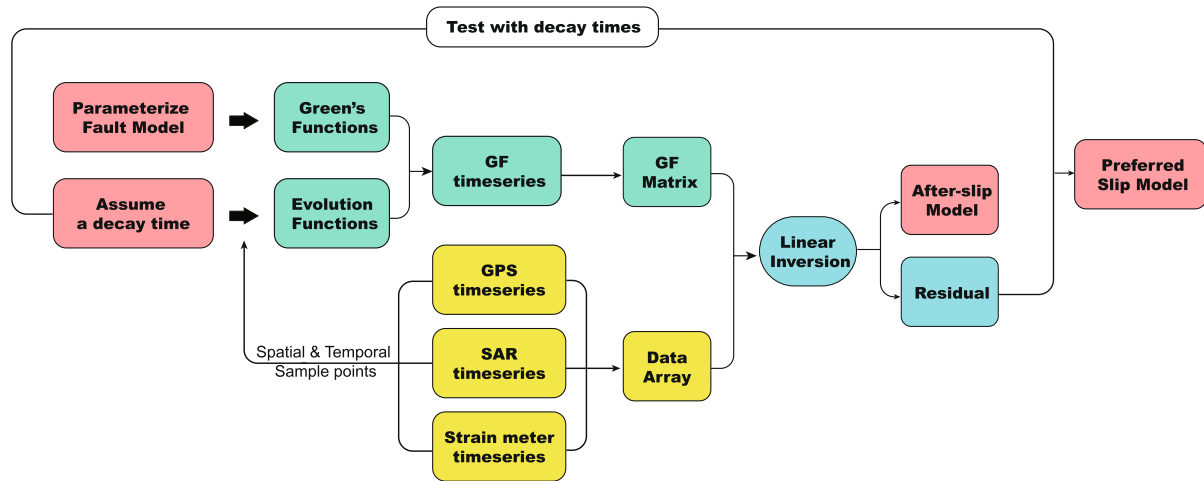


**Figure 2.** Full time-series inversion flow chart. Model, Green's function, and data are marked as red, green, and yellow-filled rectangles, respectively. Search for characteristic decay times is plotted as the outer-most cycle, which is used to select the preferred slip model and decay time.

$$\mathbf{u}_{j(t)} = \sum_{i=1}^n \mathbf{m}_i \mathbf{G}_{i,j} S_i(t) \quad (6)$$

where the spatial variables of  $x'$  and  $x$  denote the locations of the  $i$ th source grid and  $j$ th data point, which can be a pixel of an InSAR image or a component of GNSS/strainmeter station;  $m_i$  represents the slip or moment of the  $i$ th grid. Equation 6 shows that the temporal evolution of surface displacement at a given point  $j$  can be calculated by a linear summation with the following equation:

$$\mathbf{u}_{j(t)} = \sum_{i=1}^n \mathbf{G}_{i,j(t)} \mathbf{m}_i \quad (7)$$

where  $m_i$  represents the spatial distribution of the sources to be inverted for using the observed surface deformation (afterslip distribution in the case of afterslip);  $G_{i,j(t)} = G_{i,j} * S_{i(t)}$ , the Green's function connecting the source to observation with a unit load having multiplied with  $S$ .

For large earthquakes, the postseismic relaxation is excited by the coseismic stress change, which generally has a predictable evolution function for a given relaxation mechanism, including afterslip, poroelastic relaxation, and viscoelastic relaxation. Therefore, it is more straightforward to use a prescribed evolution function  $S(t)$  based on a mathematical representation of a given underlying relaxation mechanism when characterizing the temporal evolution of the corresponding source, instead of fully relying on the data that are often subject to large errors and uncertainties. It is shown that with a rate-and-state frictional law (e.g., Marone et al., 1991), the temporal evolution of afterslip can be well represented by a logarithmic function

$$S_i(t) = S(t, t_0, \tau_i) = \begin{cases} 0, & \text{for } t < t_0 \\ \log\left(\frac{t-t_0}{\tau_i} + 1\right), & \text{for } t > t_0 \end{cases} \quad (8)$$

where  $t_0$  is the mainshock occurring time and  $\tau_i$  is the characteristic decay time of the  $i$ th subfault. If the decay time does not vary significantly over the fault plane or the data lack resolution to discriminate its spatial variation, one can assume a uniform decay time for the entire fault hosting the afterslip. Assuming an analytical source evolution function is the key operation of the FTI method, which linearizes the inversion problem and accommodates various temporal sampling of different data sets. For any given data set, the sampling times are known, thus the analytical function of Equation 8 enables the Green's function time series to be calculated for any temporal samplings (Figure 2). This ensures that the data acquired at different sampling rates (e.g., secondly, daily, and weekly) can be included in FTI.

The form of the FTI algorithm simply resembles that of any linear inversion

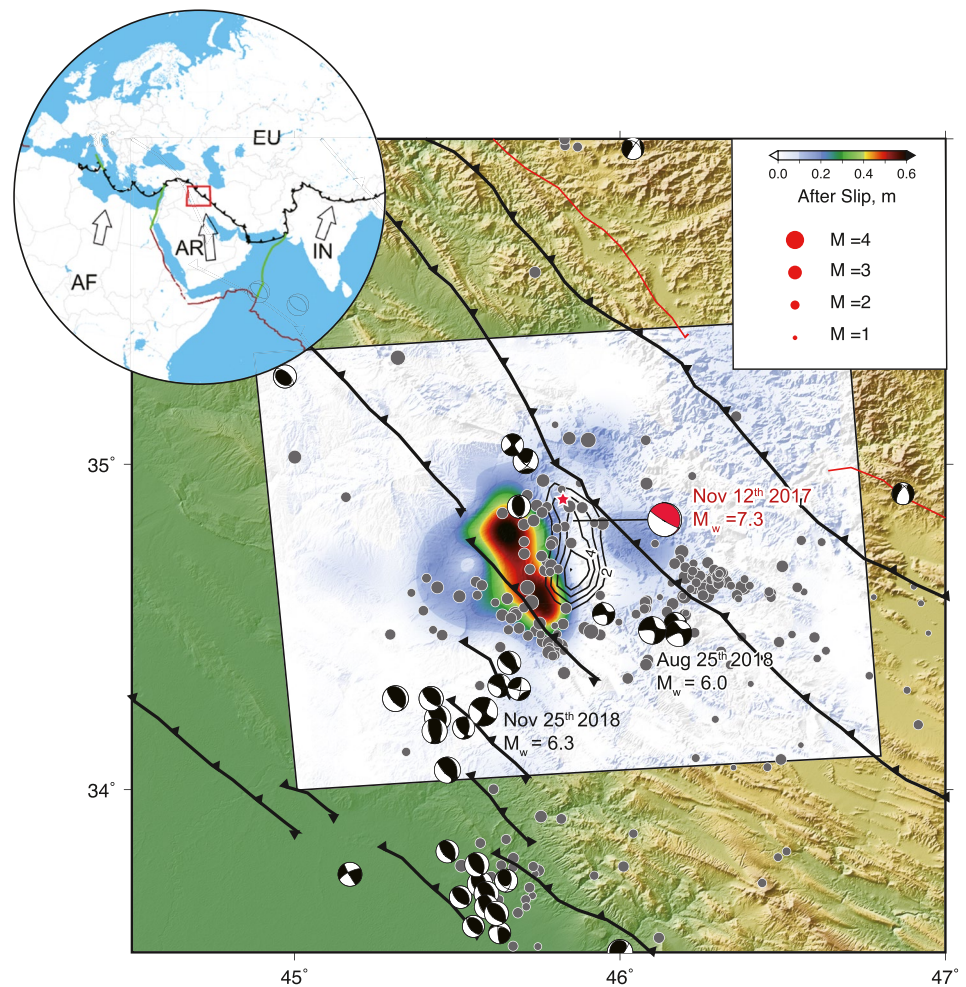


**Figure 3.** Tectonic setting of the 2017 Sarpol-e Zahab earthquake. The inset map shows location of the studied area, and the black barbed curves represent the convergent plate boundaries. In the main map, black contours represent the coseismic slip model of the mainshock from Wang and Bürgmann (2020). Color with the white-to-black spectrum indicates the magnitude of afterslip 1 year after the mainshock inferred from full time-series inversion. Focal mechanisms of regional earthquakes are plotted as black-filled beach balls. The epicenter and focal mechanisms of the mainshock are plotted as a red-filled star and beach ball, respectively. Aftershocks are plotted as gray-filled circles.

$$Gm = d \quad (9)$$

where  $G$  is a 2D matrix constructed by Green's function time series.  $d$  is the data vector simply constructed by concatenating time series data into a column vector. The column element of  $G$  and  $d$  should represent the same spatial location at the same time.  $m$  is the slip/moment components of each subfault concatenated in an array. The discretization of a fault model is identical to that of the traditional finite fault inversion, which can use a single slip at a given rake angle or slip along two perpendicular directions to perform full-linear or non-negative linear inversions. The whole FTI inversion architecture is summarized in Figure 2. Fault geometry and SEF of the source are presumed before performing the inversion. The spatial location and temporal samples of all available data are used to calculate Green's functions and SEF, which are then used to construct Green's function time series and inversion matrix. The spatial distribution of an afterslip model  $\mathbf{m}$  can be directly obtained by a linear inversion, while its evolution function needs to be computed with the assumed SEF via the equation  $\mathbf{m}_{i(0)} = \mathbf{m}_i * \mathbf{S}_{(0)}$ . In the case of afterslip, the task becomes to explore the spatial distribution of afterslip and characteristic decay time  $\tau_i$  in Equation 8 that can best explain the observed surface deformation time series. The simplest case is that all afterslip patches are assumed to have the same SEF, and thus the same value of  $\tau_i$  for all patches. The optimal value of  $\tau_i$  can be found by the grid search method so that it minimizes the difference between the model-predicted and observed surface deformation time series (Figure 2).

The above architecture describes inversion with a single decay time for afterslip on the entire fault plane. If the data indicate a spatial variation of decay times, one can parameterize each subfault with multiple decay times to perform a similar inversion. This strategy assumes that the SEF of each subfault is a linear summation of multiple functions with different values of  $\tau_i$  in Equation 8, and the total afterslip model can be computed by summing up the models of different decaying times. This resulting afterslip evolution, however, may exhibit high-order variations that cannot be fully characterized by the logarithmic function predicted by the rate-strengthening friction (RSF) model (Equation 8), if the fault patches with different SEF functions are spatially overlapping. In such cases, the summation of multiple SEFs may produce a higher order of variation that deviates from the hypothetical logarithmic function. This generally requires that the data have good spatial and temporal coverages with a relatively low noise level so that the spatial variation in the decaying times can be well resolved. For example, if the surface deformation is suggestive of distinct evolution functions (SEF) for afterslip up- and down-dip portions of the coseismic rupture, one can parameterize the up- and down-dip parts of the fault as two faults and search for their respective decaying times. A grid-search strategy similar to single process inversion can be realized by performing FTI for different combinations of decay times, and the optimal decay times can then be selected from a two-dimensional residual distribution. The 2D grid search is also the primary algorithm that we use to search for the characteristic decay times of afterslip following the 2017 Sarpol-e Zahab earthquake. Both source parameterizations are tested in the synthetic test section. Below we briefly summarize the merit of the FTI for a particular application in afterslip inversions. A detailed description of the FYI can also be found in Yue et al. (2021).

1. The FTI can flexibly incorporate different types of surface deformation measurements in a joint inversion. For the case of the Ridgecrest earthquake, the duration of strainmeter recordings (2 days) is shorter than the sampling interval of available InSAR data (6 days). The lack of temporal overlapping in data acquisition times between the different data types makes it difficult for employment of the PCA or NIF methods, while FTI does not have this limitation.
2. In comparison with the static afterslip inversion with displacements between discretized time epochs, using full time series can potentially reduce the model uncertainties. The FTI uses all sample points to estimate the parameters in the assumed SEF. It is, therefore, less sensitive to observational errors in comparison with inversion with segmented data. This advantage is demonstrated in the synthetic tests below.
3. The FTI can handle slow-slip processes with variable SEFs. Practically, the inversion procedure can start with a single process parameterization. Extra or separated processes can be added to subfaults associated with large residuals to test if the residual can be explained by additional processes. This property makes it straightforward to simultaneously consider the relaxation processes due to large aftershocks in the inversion too. In such cases, additional fault planes and step-like SEFs can be added to the SEF of the mainshock to accommodate the possible contributions from large aftershocks. This is an important strategy to isolate contributions of large aftershocks, which enables better estimation of afterslips.

In this paper, we only focus on afterslip inversion, although the FTI, in theory, can also be used to investigate the transient deformation due to other mechanisms, for example, volumetric deformation sources related to viscous relaxation and pore-fluid migrations. For such sources, the in-elastic volume deformation can be computed with strain sources distributed in a volume to form the basis of Green's function (Barbot & Fialko, 2010). With analytical solutions of volumetric deformation sources (e.g., Barbot et al., 2017) and characteristic SEF of viscous and poroelastic processes (e.g., Barbot & Fialko, 2010), we can cover all three commonly considered postseismic relaxation mechanisms in FTI, including afterslip on faults, viscoelastic relaxation in the bulk lower crust and upper mantle, and poroelastic rebound in the upper crust to perform a simultaneous inversion. Incorporating different relaxation mechanisms in a joint inversion provides a possible strategy to investigate various mechanical properties of the fault and surrounding lithosphere using postseismic deformation observations (e.g., Moore et al., 2017). In Yue et al. (2021), the contribution of surface deformation from viscous relaxation was removed before the FTI exploration, while future studies may need a more complete discussion about the possibility of including other mechanisms.

## 2.2. Initial and Orbit Corrections for SAR Data

InSAR data need a special correction in the FTI. In the inversion, the InSAR data are catenated in a 1D array to enable linear inversion. Conventional InSAR time series analysis methods, such as Small Baseline Subset (SBAS) commonly assume zero displacements at the time of the first SAR image acquisition. For postseismic deformation studies, this corresponds to the time of first postseismic image acquisition, which is often hours to days after

mainshock. In FTI, InSAR displacements are converted to a motion relative to the first epoch, thus the displacement of the first data epoch is zero. Synthetic ground displacements are generated at all epochs, from which the initial displacement is removed to recover relative displacements. Theoretically, fitting synthetic and observed relative displacements obtains an identical result as using absolute displacements. Despite of various corrections applied, the derived InSAR time series may still contain errors due to various factors, for example, the residual atmospheric noise. The SBAS algorithm, however, assumes it to be zero at all pixels. Such a simplification may result in the observation error of the first time epoch being propagated into subsequent time epochs. This “systematic error” in all epochs could bias the inversion results. To correct for this bias, we estimate the errors of each pixel in the first epoch together with slip parameters. A new inversion matrix is thus constructed as follows:

$$\mathbf{G}_{mat} = [\mathbf{G}_{slip}, \mathbf{G}_{ini}] \quad \text{and} \quad \mathbf{m} = \begin{bmatrix} \mathbf{m}_{slip} \\ \mathbf{m}_{ini} \end{bmatrix} \quad (10)$$

where  $\mathbf{G}_{slip}$  is the matrix built up by slip Green's functions.  $\mathbf{G}_{ini}$  is the matrix used to correct for initial image errors, which has a dimension of data number  $\times$  pixel number. The  $i$ th column of  $\mathbf{G}_{ini}$  is set to be one for temporal elements related to the  $i$ th pixel. The  $i$ th element of  $\mathbf{m}_{ini}$  depicts the correction (observational error) of the  $i$ th pixel of first epoch.  $\mathbf{G}_{ini} * \mathbf{m}_{ini}$  thus add  $\mathbf{m}_{ini}$  to all epochs of the  $i$ th pixel. The dimension of  $\mathbf{m}_{ini}$  is identical to the pixel number.

InSAR data often contain large-scale ramp-like errors due to the inaccuracy of satellite orbits or atmospheric noise. For FTI with InSAR time series, we adopt a similar correction in the inversion matrix ( $\mathbf{G}_{ramp}$ ) to simultaneously account for these possible large-scale errors related to orbital ramps and/or unmodeled large-scale atmospheric noise. The ramp correction can be estimated with a constant (one parameter), linear (three parameters), and quadratic ramp (six parameters) signals using phase values observed at different pixel locations. Pixel location-related corrections ( $\mathbf{G}_{ramp}$ ) are constructed using a similar strategy as  $\mathbf{G}_{ini}$ . However, we note that the orbital ramp errors in Sentinel-1 data are generally small enough to be neglected.

Finally, the equation accounting for the errors due to reference time difference and large-scale ramps in InSAR can be written as

$$\mathbf{G}_{slip} \times \mathbf{m}_{slip} + \mathbf{G}_{ini} \times \mathbf{m}_{ini} + \mathbf{G}_{ramp} \times \mathbf{m}_{ramp} = \mathbf{d} \quad (11)$$

which is presented as a matrix production as  $\mathbf{G}_{mat} * \mathbf{m} = \mathbf{d}$ , where

$$\mathbf{G}_{mat} = [\mathbf{G}_{slip}, \mathbf{G}_{ini}, \mathbf{G}_{ramp}] \quad \text{and} \quad \mathbf{m} = \begin{bmatrix} \mathbf{m}_{slip} \\ \mathbf{m}_{ini} \\ \mathbf{m}_{ramp} \end{bmatrix} \quad (12)$$

One issue of including the initial and ramp correction is that such parameterization is incompatible with non-negative constraints. For many source inversions, non-negative least-square inversion, (e.g., Lawson & Hanson, 1995), is commonly adopted to only allow for slips in the direction that is compatible with the prevailing stress direction for a given fault. However, including both slip and InSAR corrections in a simultaneous inversion prevents the inversion from exploring the negative domain of correction parameters. To solve such a problem, we also include negative initial and ramp correction matrix ( $\mathbf{G}_{ini}^-$  and  $\mathbf{G}_{ramp}^-$ ) in the inversion matrix, which is simply reversing the sign of  $\mathbf{G}_{ini}$  and  $\mathbf{G}_{ramp}$ , and this operation produces a matrix form as

$$\mathbf{G}_{mat} = [\mathbf{G}_{slip}, \mathbf{G}_{ini}^+, \mathbf{G}_{ramp}^+, \mathbf{G}_{ini}^-, \mathbf{G}_{ramp}^-] \quad \text{and} \quad \mathbf{m} = \begin{bmatrix} \mathbf{m}_{slip} \\ \mathbf{m}_{ini}^+ \\ \mathbf{m}_{ramp}^+ \\ \mathbf{m}_{ini}^- \\ \mathbf{m}_{ramp}^- \end{bmatrix} \quad (13)$$

Non-negative estimation of  $\mathbf{m}^+$  and  $\mathbf{m}^-$  allows for the solution to have both positive and negative values. However, because  $\mathbf{G}^+$  and  $\mathbf{G}^-$  matrices are fully correlated, catenating them makes the whole matrix under-determined. Such

conditions introduce the non-uniqueness of correction parameters. For instance, any constant added to  $m^+$  and  $m^-$  produces identical fits to the data, because its contribution to the data fitting is canceled by the  $G^+$  and  $G^-$  terms. To solve the non-uniqueness problem, we add further constraints to the corrections parameters, which constrains

$$Damp\_ini \times (m_{ini}^+ + m_{ini}^-) = 0 \quad (14)$$

$$Damp\_ramp \times (m_{ramp}^+ + m_{ramp}^-) = 0 \quad (15)$$

Equations 14 and 15 damp the total amplitude of correction parameters, thus reducing the instability of corrections. Similar operations are also used in tomography model stability controls, and the level of damping parameters can be selected using a similar “L-curve” strategy as spatial smoothing dampers. Another criterion of  $D_{amp\_ini}$  can be selected by recovering  $m_{ini}$  to be comparable to the noise level (residuals) of other epochs.

### 2.3. Synthetic Tests

To validate the performance of FTI, we use controlled synthetic tests to check if FTI can resolve the spatial distribution of given sources and SEF. For demonstration purposes, here we only consider afterslip as the source. We carry out two tests. One model assumes that the afterslip occurs on a fault area with uniform SEF (hereafter referred to as the single-process test). The other model has two different temporal evolution functions for different portions of the fault (hereafter referred to as the two-process test).

### 2.4. Single Process Synthetic Test

We first set up a  $40 \times 40$  km fault plane that strikes to the north and dips to the east with a low dipping angle of  $5^\circ$ . The input afterslip is assumed to take place across the entire fault plane with a  $10 \times 10$  km scale checker-board slip pattern. For such shallow dipping faults, deformation from different portions of the fault has limited spatial overlap, thus the trade-off between up- and down-dip slip in the model is low. Ground displacements are generated at 24 synthetic GNSS stations, located at 10, 20, and 30 km from the center of the fault plane with  $45^\circ$  azimuth increment (Figure S1 in Supporting Information S1). InSAR line-of-sight (LOS) displacements are generated above the fault plane with 4 km spacing for both ascending and descending orbits. We assume a uniform SEF over the entire fault plane with a characteristic decay time of  $\tau = 10$  days in Equation 8. GNSS and InSAR time series are generated with 1-day and 6-day intervals, respectively.

We also add synthetic random noise with temporal and spatial correlations to the GNSS and InSAR data, respectively. A running box-car filter of 3-day width is applied to the GNSS noise time series to introduce a temporal correlation. For the InSAR data, we generate synthetic noise assuming a power-law spectrum density distribution where the energy is inversely proportional to the frequency, meaning that the noise is most prominent at relatively long wavelengths (Li et al., 2007; Williams et al., 1998). The correlation distance is about 10 km resembling the troposphere noise commonly seen in real interferograms. A noise level of up to 20% of the total displacement is added to the synthetic LOS displacements. The same level of orbital ramp error is also added, although the orbital error in the Sentinel-1 data is seemingly very small. Both FTI and static inversion are performed, whereas the static inversion only uses displacements between the last and first SAR acquisitions. Comparisons between input and inverted results are shown in Figure 4.

With such a high noise level, FTI clearly outperforms the static inversion. This is mainly because the FTI takes advantage of the full time series while the static inversion relies on data at only selected epochs, which can be easily contaminated by noise at the time epochs when the data are used to estimate the cumulative displacements. The spatial resolution of slip in both models decreases with depths, which is a common problem in the inversion of fault slip using surface displacements. The input decay time can also be picked from the residual trade-off curve (Figure S2 in Supporting Information S1).

In the synthetic test, we use uniform weighting for all sampled InSAR data points, which makes the inversion more straightforward when incorporating data from different satellite orbits. We also test a weighting scheme where the noise is spatially correlated following the equation:

$$Corr = a \exp(-dist/b) \quad (16)$$

where  $dist$  is the spatial distance between any two pixels;  $a$  represents the characteristic noise level, and  $b$  the characteristic correlation distance. In the synthetic test, for any given realization of noise,  $a$  and  $b$  can be found

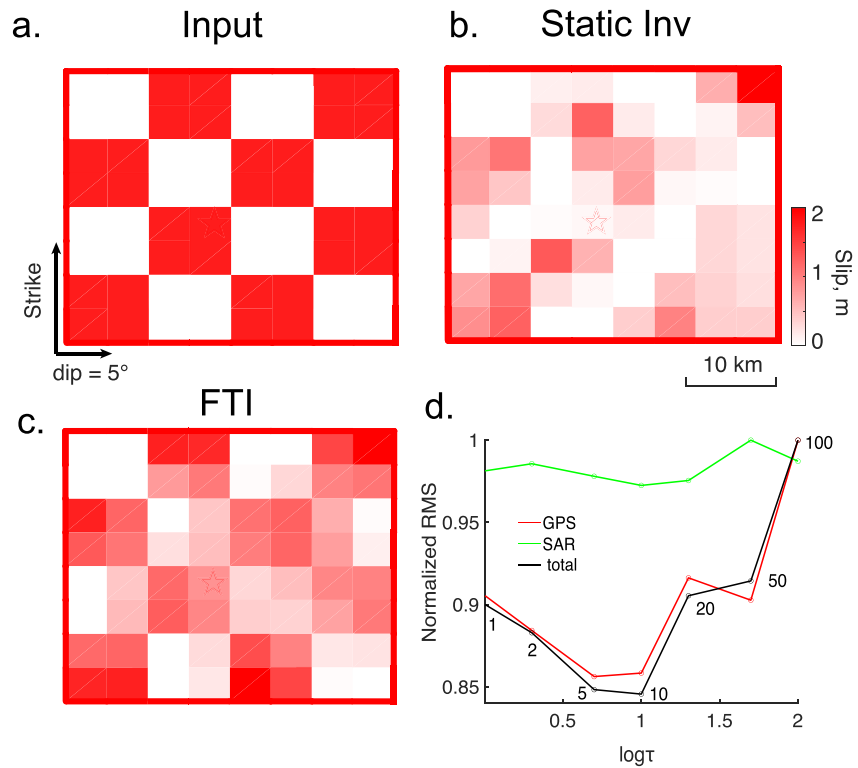


**Figure 4.** Synthetic test of full time-series inversion (FTI) for afterslip with a single process. (a) Input afterslip model; (b) pattern of afterslip from static slip inversion; and (c) pattern of afterslip from FTI inversion. Slips on each subfault are plotted using the same white-red color scale. (d) Model misfit as a function of the decay time  $\tau$  describing the rate of the afterslip's temporal evolution.

by fitting the noise sampled at different locations using the above equation, which can be then used to calculate the data covariance matrix ( $C_d$ ). In this setup, the off-diagonal components of  $C_d$  are non-zero, which introduces spatial correlation between data samples. The inverse of spatial correlated  $C_d$  is then used to weight  $\mathbf{G}_{\text{mat}}$  and  $\mathbf{d}_{\text{mat}}$  to perform a linear inversion. The cost function including the covariance matrix is written as

$$\text{Obj} = \| (\mathbf{G}_{\text{mat}} \mathbf{m} - \mathbf{d}_{\text{mat}}) \mathbf{C}_d^{-1} (\mathbf{G}_{\text{mat}} \mathbf{m} - \mathbf{d}_{\text{mat}}) \|_2 \quad (17)$$

For the inversion with real data sets  $a$  and  $b$  in Equation 16 can be estimated by fitting the residual displacement field after subtracting the prediction from a preliminary model. In such cases, similar to the synthetic test, the covariance matrix  $C_d$  has non-zero off-diagonal components. However, we note that the spatial correlation only exists between sampled LOS displacements of the same time epoch from the same satellite orbit. That is, we do not consider the temporal correlation in the InSAR data. Under these assumptions,  $C_d$  is a very sparse matrix that only blocks of elements near the diagonal are not zero, which makes the operation of the  $C_d$ , including contrasting, saving, and inverting quite computationally efficient.

We tested FTI with synthetic InSAR data with and without spatial correlation, where the off-diagonal components of the covariance matrix  $C_d$  are zero and non-zero, respectively. A comparison of the respective results is shown in Figure S5 in Supporting Information S1. Although the result suggests that including the spatial correlation in the data better recovers the downdip slip pattern, a similar improvement in resolution can be also achieved by reducing the smoothing factor. Thus, the merit of including spatial correlation of noise is not obvious in our test. We also performed a similar test with real data by including the spatial correlation between data points. The resulting slip model had marginal difference compared to the one without.

### 2.5. Double Process Synthetic Test

We then test the model with different SEFs across the fault. Slip of characteristic relaxation times of  $\tau_1 = 5$  days and  $\tau_2 = 100$  days are prescribed on the up- and downdip portion of the fault, respectively (Figure 5). Cumulated

displacement in the up- and downdip portions are about 1 and 2 m, respectively. Such a fault geometry and slip configuration are chosen to mimic the fault geometry and afterslip evolution following the 2017  $M_w$  7.3 Sarpol-e Zahab earthquake, for which the afterslip is found to occur both up- and downdip of the coseismic rupture, but with different relaxation times (Wang & Bürgmann, 2020). Since the primary goal here is to test if the FTI can well resolve the afterslip of different spatial and temporal characteristics, the model does not include the fault segment that ruptured during the coseismic phase and separated the updip and downdip afterslip zones. The ground displacements are computed at the same GNSS and InSAR points as those in the single process test.

We conducted two sets of FTI inversions, namely, the double-process test and the separated double processes test. For the double-process test, we parameterize all subfaults with the same two logarithmic functions. For the separate double process, we parameterize the up- and downdip faults with separate logarithmic functions and different characteristic decay times. Similar to the single-process case, the characteristic decay times are determined in a 2D grid search in both tests.

For both cases, the FTI can recover both spatial and temporal distributions of the input slip reasonably well (Figure 4). However, for the double process inversion, the inferred updip slip ( $\tau_1 = 5$  days) is smeared into the downdip patch. This artifact may originate from the fact that afterslip near the junction of two slip patches with different decay times contribute comparably to the surface deformation, making the separation of slip in space difficult, particularly when the data contain strong noise. Nonetheless, when considering the general slip behavior of two main slip patches, the result clearly shows that they are characterized by different SEFs. One drawback of the FTI in the exploration of afterslip is that it is unclear if the combination of multiple logarithmic functions can still match the predictions from an RSF model, which is critical to analyze the frictional properties of the fault near the junction of slip patches. Thus, if the inverted afterslip model includes multiple areas of apparently significant slip, it may be more appropriate to invert for the decay time of each patch with variable SEFs. This is also the inversion scheme adopted for the 2017 Sarpol-e Zahab earthquake, which is described in more details as below.

### 2.5.1. Application to the 2017 ( $M_w = 7.3$ ) Sarpol-e Zahab Earthquake

The method FTI was first introduced and applied to explore afterslip evolution following the 2019 Ridgecrest earthquake sequence (Yue et al., 2021), where a double-process inversion scheme is employed. However, the estimated parameter of the second process in the Ridgecrest case appears to be sensitive to a strainmeter station located near the main rupture. Therefore, the performance for double slip processes is not well demonstrated in that study. In this study, we choose the 2017  $M_w$  7.3 Sarpol-e Zahab earthquake to evaluate the performance of double slip process for FTI, because a previous study has identified afterslip in both up- and downdip around the coseismic rupture, showing distinct evolution functions (Wang & Bürgmann, 2020). These characteristics make it ideal to test the performance of FTI.

## 2.6. Data and Model Setup

InSAR data used here are from Wang and Bürgmann (2020), which include LOS displacement time series derived from Sentinel-1 data from two ascending and two descending orbits. Information of the InSAR data is summarized in Table 1.

Details of SAR time series processing are available in Wang and Bürgmann (2020). We resampled the processed data of Wang and Bürgmann (2020) at slightly larger spatial bins to enable more efficient inversion in FTI. Although the InSAR analysis of Wang and Bürgmann (2020) involves advanced atmospheric noise reduction, the resulting time series still exhibit large variations at certain locations, particularly in areas of relatively low deformation. To enhance the SNR, we only select the pixels where the total LOS displacement is greater than 3 cm and average the LOS displacement within about 1 km at each time epoch. The resulting time series and spatial variation of the InSAR data are plotted in Figure 6. Line-of-sight displacements at 1331 pixels above the fault plane are used in the inversion. There are  $\sim 60$  SAR acquisitions for each track during the  $\sim$ one year period, corresponding to a 6-day revisit interval. The rectangular fault plane of 150 km along strike and 180 km along dip is divided into  $15 \times 18$  subfaults along each direction, respectively. We use the same fault geometry as Wang and Bürgmann (2020), in which the dip angle of subfaults above and beneath 15 km depth is set to be  $5^\circ$  and  $17^\circ$ , respectively.

Besides afterslip on the main fault plane, a significant aftershock of  $M_w = 6.0$  occurred on 25 August 2018, above the downdip fault portion. Focal mechanism solution suggests that this is a strike-slip event with an approximately

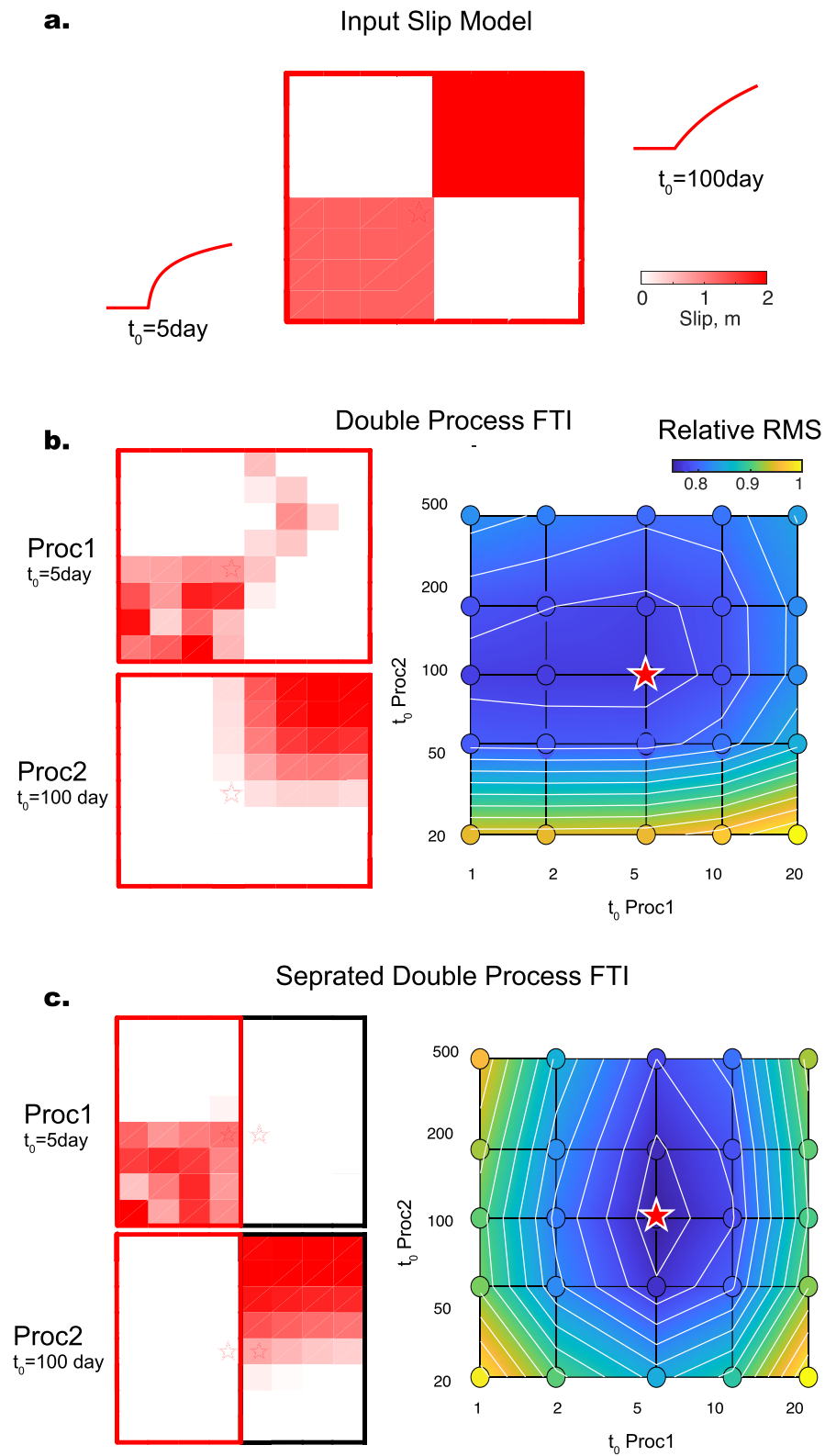


Figure 5.

**Table 1**  
*InSAR Data Used for 2017 Sarpol-e Zahab Postseismic Deformation Study*

Orbit	Start date	End date	No. epoch	No. pixel
ASC174	18 November 2017	31 December 2018	65	490
ASC72	17 November 2017	30 December 2018	68	301
DES6	19 November 2017	26 December 2018	56	270
DES79	18 November 2017	25 December 2018	61	270

E-W trending strike. Since the InSAR displacement time series of Wang and Bürgmann (2020) contains contribution of this large aftershock, the coseismic slip of this event needs to be simultaneously inverted along with the afterslip of the mainshock, to avoid its signal to influence the downdip afterslip inversion. We parameterize this fault plane with a 30 km × 15 km rectangle, which is divided into 3 km by 2 km subfaults, respectively. The strike/dip/rake angle of the aftershock fault plane is set as 265°/82°/330° concerning its GCMT solution. The geometry of the aftershock on the 25 August 2018 fault plane is set up based on the GCMT focal mechanism solution and spatial clustering of aftershocks. The SEF of the coseismic deformation of this aftershock is set as a step function at its origin time and its coseismic slip

pattern is inverted together with afterslip on the main fault plane. Elastic Green's functions are computed for each subfault using a layered half-space model (R. Wang et al., 2003), with the velocity model obtained from CRUST 1.0 (Laske et al., 2013). As described above, although the FTI allows for including orbit ramp corrections for each SAR frame, such operation is most stable if GNSS data are available to constrain the absolute displacements of each image. Unfortunately, GNSS data are not available for the Sarpol-e Zahab earthquake, so including ramp corrections may introduce an unstable estimation of evolution function parameters. Also, since orbital ramp signals are not obvious in our InSAR data, we do not include the ramp estimation in the FTI of this event.

### 2.6.1. One-Process Inversion

Similar to synthetic tests, we explore the afterslip evolution of the 2017 Sarpol-e Zahab earthquake assuming both uniform and variable SEFs. We first invert for the afterslip model using a uniform SEF over the entire fault plane. Afterslip on the main fault and the aftershock planes are parameterized with logarithmic and step functions, respectively (Figure 7). The inverted afterslip model and residual trade-off curve are plotted in Figure 7. Similar to Wang and Bürgmann (2020), the model is characterized by afterslip both updip and downdip of the coseismic rupture, with most of the moment release being concentrated in the updip portion. The maximum cumulative afterslip reaches ~0.5 m on a subfault patch updip of the coseismic rupture. The total moment of this afterslip model is equivalent to  $M_w$  6.94. The equivalent moment magnitude of the biggest aftershock on 25 August 2018, is found to be  $M_w$  6.02, which is in good agreement with the CGMT solution. An optimized decay time of  $\tau = 10$  days can be selected from the residual trade-off curve. The increment of decay time search is about a factor of two, that is, 1, 2, 5, 10, and 20 days. Because the trade-off curve varies smoothly with the decay times, we use a relatively large increment to ensure computation efficiency. Using a finer searching interval does not yield a more accurate decay time estimation, since residuals are similar for the decay time ranging between 5 and 20 days.

### 2.6.2. Two-Process Inversion

We then test the inversion with two different relaxation times for slip in the up- and downdip portions of the coseismic rupture. In this test, we divide the major fault plane into up- and downdip fault portions separated by the hypocenter. Because the updip and downdip of the coseismic rupture have limited spatial overlap, it is easy to select a depth to fully separate the two afterslip areas. The SEFs on up- and downdip fault segments are assumed to follow a logarithmic function of different characteristic decay times ( $\tau_{up}$  and  $\tau_{down}$ ).

We find that the model with  $\tau_{up} = 10$  days and  $\tau_{down} = 50$  days best fits the data. Slip patterns of the two-process inversion resemble that of the one-process inversion, with a cumulative moment of 6.87 and 6.46 for the updip and downdip regions, respectively. The total moment of the two-process afterslip model is 6.94, similar to the one-process model. The residual distribution appears to be more influenced by  $\tau_{up}$ , which is somewhat expected since the updip slip dominates the afterslip moment release. To further explore the data sensitivity to the downdip afterslip, we select the InSAR pixels above the downdip portion and plot its residual trade-off curve along the  $\tau_{up} = 10$  days residual profile. The data misfit of the downdip pixels should be more sensitive to the downdip afterslip, for which the data clearly prefer a longer decay time of ~50–200 days. This comparison suggests

**Figure 5.** Synthetic test of full time-series inversion (FTI) for afterslip with different relaxation times. (a) Spatial pattern of the input afterslip model. Note that the characteristic decay functions are different for the updip (left two subfaults) and downdip (right two subfaults) patches. (b) Inferred afterslip model obtained with. Slip patterns associated with short and long decaying processes are plotted in the top and bottom panels, respectively. Residual root mean square distribution in the decaying time domain is plotted in a blue-yellow color scale, with the optimal point marked as a red star. (c) The same as (b), but the characteristic decaying times updip and downdip portions of the fault are prescribed to be different.

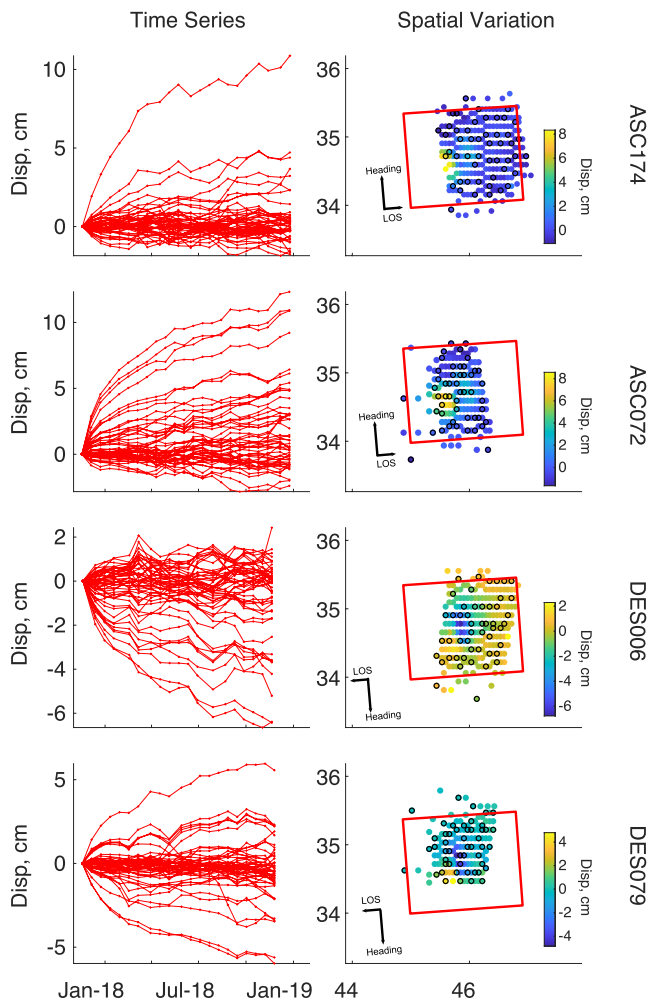


**Figure 6.** Example of postseismic Synthetic Aperture Radar Interferometry displacements following the 2017 Sarpol-e Zahab earthquake. The left and right panels show the time series and spatial variation of line-of-sight displacements of each satellite track at pixels where the total displacements are greater than 3 cm after 1 year, respectively.

that the preference for a longer decay time mainly originates from downdip pixels. Although data at part of the pixels indicate a longer decay time of 100 days, we prefer to determine the optimal downdip decay time using data at all pixels, which reduces the bias in model constraints as a result of spuriously high noise at individual locations.

The double-process inversion achieves about 62% variance reduction with respect to the observation, with a mean temporal RMS reduced from 1.3 cm in the raw data to 0.5 cm in the residuals (Figure 9). We interpolated the surface displacement field evolution and calculate the remanent displacement field. The temporal variance of observed, synthetic and residual displacements are plotted in Figure S10 in Supporting Information S1 to demonstrate the fitting of the FTI result. It is noted that some concentrated residual is presented near the surface trace of the  $M_w$  6.0 aftershock, which may be related to a coarse discretization of the fault plane for this aftershock. Though improvements might be achieved by using a finer subfault discretization, we do not realize such refinement as its impact on the displacement field fit is only limited to local scales. Introduction of the down-dip afterslip results in about 3% reduction of the variance, which is approximately 3 times smaller than the 10% variance reduction as the result of introduction of the updip afterslip. This ratio is related to the slip amplitude in the up- and downdip, respectively, which indicates that the inversion sensitivity is directly related to the slip amount. We note that the improvement in variance reduction by adding the second process is quite subtle,  $\leq 1\%$  for each orbit. Particularly, the residual between data and model for the descending orbit DES6 even increased by about 0.7% in the two-process inversion, which is not fully understood, because including extra parameters generally allows for extra freedom to reduce residuals in all images. We note that the displacements from the descending orbits (DES6 and DES9) are overall smaller than that in the ascending orbits (ASC72 and ASC174) ( $\sim 0.05$  m range increase for the descending orbits versus  $\sim 0.1$  m range decrease for the ascending orbits), which may lead to a lower SNR if the level of InSAR error itself is comparable in all orbits. A relatively low SNR may introduce a biased estimation of decay time. Furthermore, the data with relatively low SNR may result in a model that is more tightly constrained by data from one orbit, while deteriorating fitting to the data of other orbits. In summary, similar to Wang and

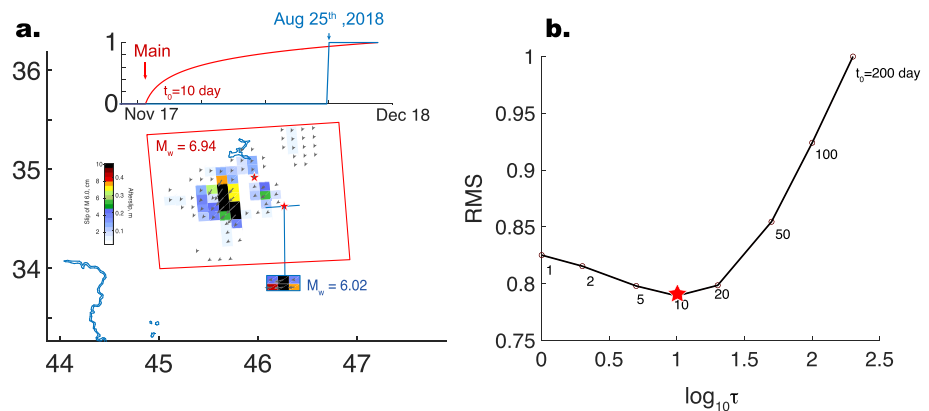


**Figure 7.** Model of afterslip following the 2017 Sarpol-e Zahab earthquake obtained with a single relaxation process. (a) Spatial distribution and temporal evolution of the afterslip. The equivalent moment magnitude of afterslip following the mainshock and coseismic moment of the M6 aftershock on 25 August 2018 are labeled. (b) Trade-off curve between residual root mean square and characteristic decay time ( $\tau$ ). The optimized decay time is marked as a red star.

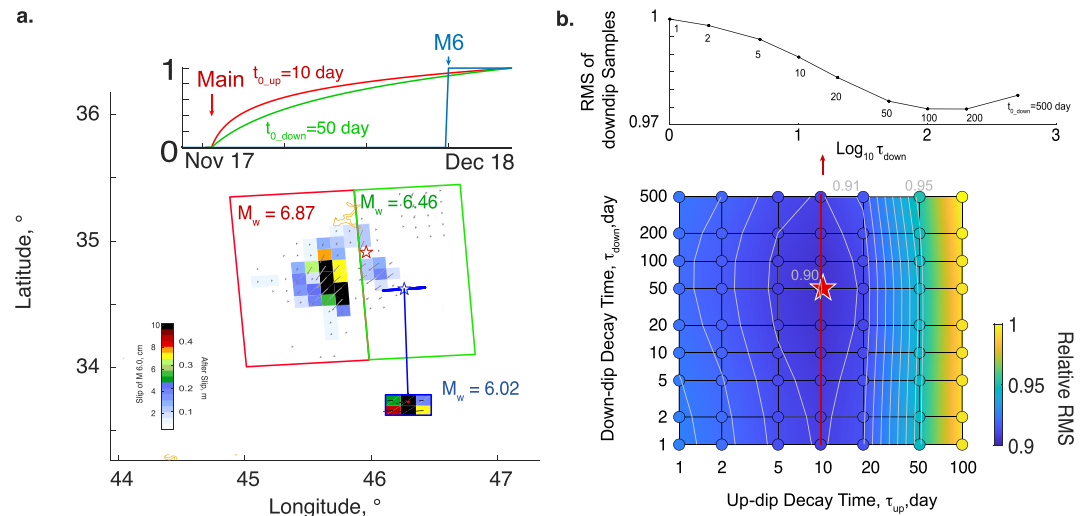


**Figure 8.** Model of afterslip following the 2017 Sarpol-e Zahab earthquake obtained with two relaxation processes. The notations in (a–c) are overall similar to Figure 7, except that in this model, the decay times of afterslip updip and downdip of the coseismic rupture have different values ( $\tau_{up} = 10$  days and  $\tau_{down} = 50$  days). (d) Residual root mean square of SAR pixels above the downdip fault portion (green box in Figure 8a) along the optimal  $\tau_{up}$  (red line) is plotted with respect to different  $\tau_{down}$  in the top panel.

Bürgmann (2020), we find that the afterslip one year after the 2017 Sarpol-e Zahab earthquake is characterized by slip both up- and downdip of the coseismic rupture. However, the FTI including a second decay time (i.e., two-process inversion) achieves marginal improvement in terms of data fitting, because of the relatively low SNR of data corresponding to the slip downdip of the coseismic rupture.

We also perform an FTI considering the spatial correlation in the InSAR data (i.e., the off-diagonal components of  $C_d$  are not zero) and compare the result with the one where  $C_d$  is assumed to be diagonal (Figure S11 in Supporting Information S1). For the FTI result with non-zero off-diagonal components in  $C_d$ , the equivalent magnitude for each process is 6.87, 6.43, and 6.01, respectively, which is close to the model assuming a zero off-diagonal  $C_d$ . The downdip slip pattern is slightly more compact in the model where the data are assumed to be spatially correlated, (Figure S11 in Supporting Information S1). Yet, whether such compactness reflects a real improvement is still subject to question, as a similar feature was also seen in the test with synthetic data sets. It is worth noting that the dimension of *dmatrix* is  $\sim 15,000$ , which is about 300 fold the parameter number ( $\sim 500$ ). In an inversion of such a scale, knowing the exact spatial correlation of noise may not influence the inversion result significantly. Considering the similarity of inversion results and the consistency of residual comparison, we used the diagonal  $C_d$  to perform FTI for all models tested in Figures 7 and 8.

### 3. Discussion

#### 3.1. Comparison With RS Modeling Results

We also compare the double process inversion results with the stress-driven afterslip model assuming a RSF that is explored in Wang and Bürgmann (2020). The RS simulation is made over a compact fault model near the coseismic slip. We make a refined slip model using the identical fault geometry as Wang and Bürgmann (2020) model, which allows for a direct comparison with their model. Separated double process FTI is adopted to realize this inversion and the comparison between the RSF modeling and FTI fine models is plotted in Figure 10. The fine sub-fault FTI result still resembles that of the coarse grid, demonstrating the stability of FTI with respect to subfault sizes. However, the FTI result is different from that obtained by RSF modeling. Assuming a uniform frictional property and pre-stress on the entire fault, the RSF modeling would yield a comparable amount of afterslip in the up- and downdip portions for a period starting from the time of main-shock, because they share a similar magnitude of the coseismic stress change. However, the observed surface deformation due to afterslip downdip of the coseismic rupture is much smaller than that of the updip. To reconcile with the observation, Wang and Bürgmann (2020) concluded that frictional properties updip of the coseismic rupture was different from that of downdip. Specifically, they indicated that the distribution

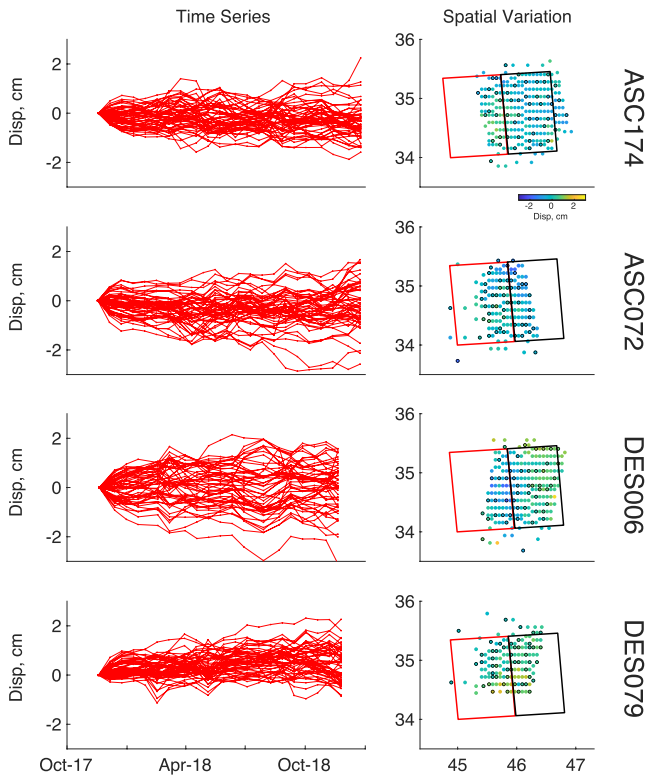


**Figure 9.** Difference between observations and model predictions of Synthetic Aperture Radar Interferometry line-of-sight displacements for different satellite tracks. The afterslip model is based on full time-series inversion with two different relaxation times (i.e., the double-process model, shown in Figure 8).

of fault friction was such that afterslip downdip of the coseismic rupture decays much faster so that when the first postseismic SAR image becomes available, much of the stress increase downdip of the coseismic rupture had been released (Figure 10b). The FTI in this study, however, prefers a slower evolution function for afterslip downdip of the coseismic rupture. Such differences may draw different implications to the frictional parameters.

The RSF modeling approach relies on prescribed frictional properties to generate the afterslip process, while FTI relies on the extrapolation of evolution functions to explore the temporal evolution of afterslip. The different strategies result in different conclusions about the downdip slip pattern for the 2017 Sarpol-e Zahab earthquake. Because early postseismic observations are not available for this event, it is hard to tightly constrain the early afterslip. The discrepancy highlights the non-uniqueness of postseismic deformation models and their dependence on different assumptions. Particularly regarding the temporal evolution functions, when observations of very early postseismic deformation are missing, different frictional property implications could be drawn. Such problems may be mitigated by including continuous GNSS and/or strainmeter measurements.

For the particular case of the 2017 Sarpol-e Zahab earthquake, FTI achieves better fits to the InSAR data in comparison with the RSF modeling. Such an improvement is expected, since FTI exploits the spatial variation of afterslip, which contains hundreds of free parameters in the inversion, while RSF modeling of Wang and Bürgmann (2020) contains a small number of free parameters: two frictional parameters ( $V_0$  and  $(a-b)\sigma$ ) updip and downdip of the coseismic rupture, respectively. Uniform initial shear stress before the mainshock is also assumed by Wang and Bürgmann (2020) to reduce the number of inversion parameters. This assumption directly leads to comparable initial stress at the beginning of postseismic processes, requiring a similar amount of total slips to be released in the whole postseismic period. However, the realistic initial stress may be significantly influenced by the distribution of creeping portions, which needs to be considered in future works.

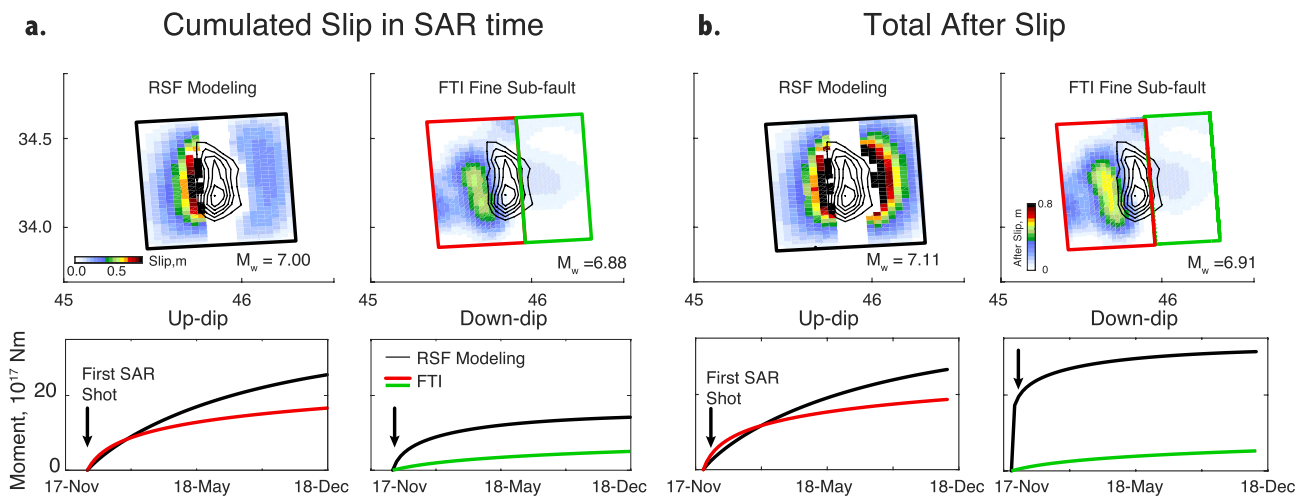


**Figure 10.** Comparison of afterslip models based on numerical simulation assuming rate-strengthening friction (RSF) law and full time-series inversion (FTI). (a) Afterslip models consistent with Synthetic Aperture Radar Interferometry data that were between 5 and 365 days after the mainshock. In the bottom row, the curves represent the temporal evolution of afterslip (shown as integrated moment release in updip and downdip afterslip regions) in the respective afterslip models; black for RSF. Red and green for the up- and downdip slip functions of FTI. The RSF afterslip model is from Wang and Bürgmann (2020). (b) The same as (a), but for total afterslips including the early afterslips. Note that the RSF afterslip model indicates a much shorter decay time for afterslip downdip of the coseismic rupture, compared to the FTI model of this study.

Liu and Xu (2019) use a LogSIM algorithm to invert the coseismic and postseismic rupture process of the 2017 Sarpol-e Zahab earthquake. They adopt a similar strategy as FTI, while their focus is to separate the coseismic slip and early afterslips by using interferograms of image pairs acquired before and after the mainshock to recover both processes simultaneously. Liu and Xu (2019) also find significant afterslip in the updip portion of the coseismic ruptures, while little to no slip is found in the area below the coseismic rupture.

FTI only obtains the afterslip deformation, which can be considered as the response of fault plane slip to an instantaneous coseismic stress change ( $\Delta\tau$ ). Under the steady-state RSF, the initial slip velocity response to a stress loading is described by:

$$\Delta V_{ss} = \frac{V_0}{(a-b)\sigma_0} \Delta\tau \quad (18)$$

(Y. Liu & Rice, 2007; Lu et al., 2022), where  $a$  and  $b$  values are the velocity strengthening and weakening parameters of RSF;  $V_0$  is the creeping velocity before the earthquake. The  $a\sigma$  value reported by Wang and Bürgmann (2020) also assumes steady state friction, which is essentially  $\sigma(a-b)$ . Wang and Bürgmann (2020) report a significant contrast of frictional parameters where  $V_0$  ( $\sim 1.5$  m/yr) and  $\sigma(a-b)$  ( $\sim 2.8$  Mpa) updip of the coseismic rupture are both 20–30 times larger than that in the downdip. We define the ratio between  $V_0$  and  $\sigma(a-b)$  as a velocity sensitivity factor and find the downdip factor is about 60% larger than that of the updip. This difference directly leads to a faster downdip stress release when comparable stress loadings are placed. The smaller total slip found in the down-dip portion of the coseismic rupture during the InSAR observation period indicates that a large portion of the motion downdip of the coseismic rupture may have been released before the first SAR acquisition, corresponding to a faster decay in afterslip downdip of the coseismic rupture (Wang & Bürgmann, 2020). The FTI result presented by this study, however, indicates a higher sensitivity in the updip portion, which presents a “faster” release of coseismic stress loading. Without precise information of pre-seismic creeping velocity ( $V_0$ ) it is difficult to conclude this discrepancy. A full frictional parameter inversion incorporating pre-, co-, and postseismic deformations should be useful to address this problem. Also, it is important to note that the SNR of the observed surface deformation due to slip downdip of the coseismic rupture is much lower. So the difference in the inferred characteristics of afterslip downdip of the coseismic rupture may simply reflect the uncertainties of these models, because of the relatively low S/N in the data. In fact, most previous studies did not resolve any afterslip downdip of the coseismic rupture.

### 3.2. Limitations and Perspectives of FTI

In this paper, we focus on testing the performance of FTI in resolving the spatial and temporal evolution of post-seismic deformation processes (mainly afterslip explored in this study) with synthetic tests and real observations of surface deformation following the 2017  $M_w$  7.3 Sarpol-e Zahab earthquake. Yet, because only InSAR data are available for this event and our algorithm is directly modified from the coseismic slip inversion, several issues remain not explored in this paper. These aspects need to be addressed with more realistic model setups and proper handling of errors and uncertainties in the data. Here, we briefly outline some of these limitations and possible strategies to improve the algorithm.

Proper handling of data uncertainties and relative weighting between data sets is important in a geophysical inversion. Ideally, if the uncertainty for each data point is well known, a covariance matrix (Cd) can be built accordingly and directly used in the inversion, which effectively serves as the weighting scheme (e.g., Duputel et al., 2014). For kinematic slip model inversion of large earthquakes, it is difficult to evaluate the theoretical and observational errors of seismic and geodetic data under the same framework, so an empirical approach is often adopted by optimizing relative weighting from residual trade-off curves of different data (e.g., Yue et al., 2020). For the FTI, geodetic data are mostly used in the inversion, which can have a direct estimation of the observation errors for constructing the covariance matrices. In this study, we tested the inversion by considering the spatial correlation of the data noise in the synthetic InSAR data sets, while ignoring the possible correlation in the temporal domain, which is introduced in filtering the time series processing to remove high-frequency noise. However, this is beyond the scope of this study, because depending on the algorithms used to construct the InSAR time series, it is not straightforward to mathematically characterize the temporal correlation of the InSAR data. In general, the relative weighting between data

sets used in FTI can be similar to that used in another more sophisticated inversion algorithm where both observation and prediction errors can be incorporated (e.g., Duputel et al., 2014; Ragon et al., 2018; Ragon & Simons, 2021).

In the design of the FTI algorithms, we emphasized the workflow to correct for the possible errors related to InSAR orbital inaccuracy and initial displacement using damping factors, while the current damping strategy is a compromise when merging FTI to our non-negative least squares inversion code. However, we note damping might not be the ideal strategy. In fact, a more flexible algorithm that solves the problem in a least-square sense with *a priori* constraints, for example, Matsu'ura and Hasegawa (1987), or the existing Python toolbox (i.e., `scipy.optimize`) can place respective bounds on the slip, initial and orbit parameters. For the purpose of this paper, reconstructing the inversion framework is a non-trivial task to include, so incorporating more flexible inversion algorithms should be included in future works. The difference between the damping algorithm and full inversion may be compared in future studies. It is also worth noting that most of the existing SAR systems, including Sentinel-1 and ALOS-2, have very good orbital controls, producing negligible orbital errors in the resulting interferograms. However, the error caused by the assumption of zero displacement in the first image acquisition of a SBAS-type InSAR time series analysis should be considered.

In this study, we explored the possibility of resolving various characteristic time scales of afterslip on different portions of a fault. We adopt an empirical approach by adding extra decay times to evaluate its improvements in fitting the data. This approach may resolve the spatial variation of decay times in afterslip when the data resolution is good enough. However, since the interaction between close by subfaults may produce extra stress loading on each other, the method may yield different decay times on these fault portions even if they have identical frictional properties. Although the model can be parameterized in such a way that each subfault has its own decay time, it is more reasonable to reduce the number of unknown parameters by assuming a uniform decay time for spatially closed subfaults limited by data resolution. Extra information from the afterslip numerical modeling may determine theoretical or empirical relationships between afterslip amount and the associated decay time. Such information can be used to pre-determine the spatial variation of characteristic decay times of FTI to enable more efficient inversion. Besides the major afterslip triggered by the coseismic stress loading, other fault behaviors, for example, spatial migration of afterslips (Jiang et al., 2021; Lengliné et al., 2012), triggered slow-slip events (e.g., Rolandone et al., 2018; Wallace et al., 2017), are also important to understand the spectrum of seismic and aseismic interaction dynamics. The current FTI algorithm cannot deal with such complex source processes; special treatment to the SEF needs to be conducted to enable such flexibility.

#### 4. Conclusions

In this paper, we described the theory and discretization method of the FTI algorithm and tested the performance of FTI in resolving the spatial and temporal evolution of afterslip with a series of synthetic and real data sets following the 2017 Sarpol-e Zahab earthquake. The main conclusions include:

1. The FTI can accommodate data sets of different spatial and temporal resolutions in a joint inversion architecture, which is benefited from the analytically assumed evolution functions.
2. FTI is capable of combining the spatial and temporal resolution of different data sets. It can also discriminate distinct afterslip patches with different evolution functions.
3. In the application of FTI to the 2017 Sarpol-e Zahab earthquake, the FTI reveals a different, yet more stable estimation of afterslip downdip of the coseismic rupture, compared to the previous stress-driven modeling effort assuming RSF. Lacking high-temporal sampling data reduces the resolution to robustly determine the evolution of early postseismic afterslip, which highlights the importance of continuous and high-rate geodetic measurements, for example, GNSS and strainmeter data.

#### Data Availability Statement

Computational programs are coded with Matlab. The inversion uses Sentinel-1 satellite data. The InSAR data used in this study are from Wang and Bürgmann (2020), which are available at <https://zenodo.org/record/4025068#.YiVgBi-B3VD>. The coding of FTI uses Matlab. Figures are mostly plotted with General Mapping Tool.

### Acknowledgments

This project is supported by the National Science Foundation of China (Grant No. 42021003).

### References

- Agnew, D. C. (1986). Strainmeters and tiltmeters. *Reviews of Geophysics*, 24(3), 579–624. <https://doi.org/10.1029/rg024i003p00579>
- Aki, K., & Richards, P. G. (2002). Quantitative seismology.
- Barbot, S., & Fialko, Y. (2010). A unified continuum representation of post-seismic relaxation mechanisms: Semi-analytic models of afterslip, poroelastic rebound and viscoelastic flow. *Geophysical Journal International*, 182(3), 1124–1140. <https://doi.org/10.1111/j.1365-246x.2010.04678.x>
- Barbot, S., Moore, J. D., & Lambert, V. (2017). Displacement and stress associated with distributed anelastic deformation in a half-space. *Bulletin of the Seismological Society of America*, 107(2), 821–855. <https://doi.org/10.1785/0120160237>
- Bedford, J., Moreno, M., Baez, J. C., Lange, D., Tilmann, F., Rosenau, M., et al. (2013). A high-resolution, time-variable afterslip model for the 2010 Maule Mw = 8.8, Chile megathrust earthquake. *Earth and Planetary Science Letters*, 383, 26–36. <https://doi.org/10.1016/j.epsl.2013.09.020>
- Berardino, P., Fornaro, G., Lanari, R., & Sansosti, E. (2002). A new algorithm for surface deformation monitoring based on small baseline differential SAR interferograms. *IEEE Transactions on Geoscience and Remote Sensing*, 40(11), 2375–2383. <https://doi.org/10.1109/tgrs.2002.803792>
- Bürgmann, R., Rosen, P. A., & Fielding, E. J. (2000). Synthetic aperture radar interferometry to measure Earth's surface topography and its deformation. *Annual Review of Earth and Planetary Sciences*, 28(1), 169–209. <https://doi.org/10.1146/annurev.earth.28.1.169>
- Cakir, Z., Chaballier, J.-B. d., Armijo, R., Meyer, B., Barka, A., & Peltzer, G. (2003). Coseismic and early post-seismic slip associated with the 1999 Izmit earthquake (Turkey), from SAR interferometry and tectonic field observations. *Geophysical Journal International*, 155(1), 93–110. <https://doi.org/10.1046/j.1365-246x.2003.02001.x>
- Diao, F., Wang, R., Wang, Y., Xiong, X., & Walter, T. R. (2018). Fault behavior and lower crustal rheology inferred from the first seven years of postseismic GPS data after the 2008 Wenchuan earthquake. *Earth and Planetary Science Letters*, 495, 202–212. <https://doi.org/10.1016/j.epsl.2018.05.020>
- Duputel, Z., Agram, P. S., Simons, M., Minson, S. E., & Beck, J. L. (2014). Accounting for prediction uncertainty when inferring subsurface fault slip. *Geophysical Journal International*, 197(1), 464–482. <https://doi.org/10.1093/gji/ggt517>
- Fielding, E. J., Lundgren, P. R., Bürgmann, R., & Funning, G. J. (2009). Shallow fault-zone dilatancy recovery after the 2003 Bam earthquake in Iran[J]. *Nature*, 458(7234), 64–68. <https://doi.org/10.1038/nature07817>
- Floyd, M. A., Walters, R. J., Elliott, J. R., Funning, G. J., Svarc, J. L., Murray, J. R., et al. (2016). Spatial variations in fault friction related to lithology from rupture and afterslip of the 2014 South Napa, California, earthquake. *Geophysical Research Letters*, 43(13), 6808–6816. <https://doi.org/10.1002/2016gl069428>
- Fukuda, J., & Johnson, K. M. (2021). Bayesian inversion for a stress-driven model of afterslip and viscoelastic relaxation: Method and application to postseismic deformation following the 2011 MW 9.0 Tohoku-Oki Earthquake. *Journal of Geophysical Research: Solid Earth*, 126(5), e2020JB021620. <https://doi.org/10.1029/2020jb021620>
- Gualandi, A., Avouac, J.-P., Galetzka, J., Genrich, J. F., Blewitt, G., Adhikari, L. B., et al. (2017). Pre-and post-seismic deformation related to the 2015, Mw7.8 Gorkha earthquake, Nepal. *Tectonophysics*, 714, 90–106.
- Gualandi, A., Perfettini, H., Radiguet, M., Cotte, N., & Kostoglodov, V. (2017). GPS deformation related to the Mw 7.3, 2014, Papanoa earthquake (Mexico) reveals the aseismic behavior of the Guerrero seismic gap. *Geophysical Research Letters*, 44(12), 6039–6047. <https://doi.org/10.1002/2017gl072913>
- Hagberg, J. O., Ulander, L. M., & Askne, J. (1995). Repeat-pass SAR interferometry over forested terrain. *IEEE Transactions on Geoscience and Remote Sensing*, 33(2), 331–340. <https://doi.org/10.1109/36.377933>
- Hsu, Y.-J., Simons, M., Avouac, J.-P., Galetzka, J., Sieh, K., Chlieh, M., et al. (2006). Frictional afterslip following the 2005 Nias-Simeulue Earthquake, Sumatra. *Science*, 312(5782), 1921–1926. <https://doi.org/10.1126/science.1126960>
- Hsu, Y. J., Simons, M., Williams, C., & Casarotti, E. (2011). Three-dimensional FEM derived elastic Green's functions for the coseismic deformation of the 2005 Mw 8.7 Nias-Simeulue, Sumatra earthquake. *Geochemistry, Geophysics, Geosystems*, 12(7). <https://doi.org/10.1029/2011gc003553>
- Hu, Y., Bürgmann, R., Uchida, N., Banerjee, P., & Freymueller, J. T. (2016). Stress-driven relaxation of heterogeneous upper mantle and time-dependent afterslip following the 2011 Tohoku earthquake. *Journal of Geophysical Research: Solid Earth*, 121(1), 385–411. <https://doi.org/10.1002/2015jb012508>
- Janssen, V., Ge, L., & Rizos, C. (2004). Tropospheric corrections to SAR interferometry from GPS observations. *GPS Solutions*, 8(3), 140–151. <https://doi.org/10.1007/s10291-004-0099-1>
- Jeffery, G., & Sydenham, P. (1973). Stability of strain-meter mounts. *Geophysical Journal International*, 33(2), 185–193. <https://doi.org/10.1111/j.1365-246x.1973.tb01858.x>
- Jiang, J., Bock, Y., & Klein, E. (2021). Coevolving early afterslip and aftershock signatures of a San Andreas Fault rupture. *Science Advances*, 7(15), eabc1606. <https://doi.org/10.1126/sciadv.abc1606>
- Jonsson, S., Segall, P., Pedersen, R., & Björnsson, G. (2003). Post-earthquake ground movements correlated to pore-pressure transients. *Nature*, 424(6945), 179–183. <https://doi.org/10.1038/nature01776>
- King, M. A., & Williams, S. D. (2009). Apparent stability of GPS monumentation from short-baseline time series. *Journal of Geophysical Research*, 114(B10), B10403. <https://doi.org/10.1029/2009jb006319>
- Kositsky, A., & Avouac, J. P. (2010). Inverting geodetic time series with a principal component analysis-based inversion method. *Journal of Geophysical Research*, 115(B3), B03401. <https://doi.org/10.1029/2009jb006535>
- Larson, K. M., Bilich, A., & Axelrad, P. (2007). Improving the precision of high-rate GPS. *Journal of Geophysical Research*, 112(B5), B05422. <https://doi.org/10.1029/2006jb004367>
- Laske, G., Masters, G., Ma, Z., & Pasyanos, M. (2013). Update on CRUST1.0—A 1-degree global model of Earth's crust, paper presented at Geophys. res. abstr.
- Lawson, C. L., & Hanson, R. J. (1995). *Solving least squares problems*. SIAM.
- Lengliné, O., Enescu, B., Peng, Z., & Shiomi, K. (2012). Decay and expansion of the early aftershock activity following the 2011, Mw9.0 Tohoku earthquake. *Geophysical Research Letters*, 39(18). <https://doi.org/10.1029/2012gl052797>
- Li, Z. (2005). *Correction of atmospheric water vapour effects on repeat-pass SAR interferometry using GPS, MODIS and MERIS data*. University of London, University College.
- Li, Z. W., Ding, X. L., Huang, C., Zou, Z. R., & Chen, Y. (2007). Atmospheric effects on repeat-pass InSAR measurements over Shanghai region. *Journal of Atmospheric and Terrestrial Physics*, 69(12), 1344–1356. <https://doi.org/10.1016/j.jastp.2007.04.007>

- Lin, Y.-N., Sladen, A., Ortega-Culaciati, F., Simons, M., Avouac, J. P., Fielding, E. J., et al. (2013). Coseismic and postseismic slip associated with the 2010 Maule Earthquake, Chile: Characterizing the Arauco Peninsula barrier effect. *Journal of Geophysical Research: Solid Earth*, *118*(6), 3142–3159. <https://doi.org/10.1002/jgrb.50207>
- Liu, X., & Xu, W. (2019). Logarithmic model joint inversion method for coseismic and postseismic slip: Application to the 2017 Mw 7.3 Sarpol Zahab earthquake, Iran. *Journal of Geophysical Research: Solid Earth*, *124*(11), 12034–12052. <https://doi.org/10.1029/2019jb017953>
- Liu, Y., & Rice, J. R. (2007). Spontaneous and triggered aseismic deformation transients in a subduction fault model. *Journal of Geophysical Research*, *112*(B9), B09404. <https://doi.org/10.1029/2007jb004930>
- Lu, W., Zhou, Y., Zhao, Z., Yue, H., & Zhou, S. (2022). Aftershock sequence of the 2017 Mw 6.5 Jiuzhaigou, China earthquake monitored by an AsA network and its implication to fault structures and strength. *Geophysical Journal International*, *228*(3), 1763–1779. <https://doi.org/10.1093/gji/ggab443>
- Marone, C. J., Scholtz, C., & Bilham, R. (1991). On the mechanics of earthquake afterslip. *Journal of Geophysical Research*, *96*(B5), 8441–8452. <https://doi.org/10.1029/91jb00275>
- Massonnet, D., Rossi, M., Carmona, C., Adragna, F., Peltzer, G., Feigl, K., & Rabaute, T. (1993). The displacement field of the Landers earthquake mapped by radar interferometry. *Nature*, *364*(6433), 138–142. <https://doi.org/10.1038/364138a0>
- Matsu'ura, M., & Hasegawa, Y. (1987). A maximum likelihood approach to nonlinear inversion under constraints. *Physics of the Earth and Planetary Interiors*, *47*, 179–187. [https://doi.org/10.1016/0031-9201\(87\)90076-8](https://doi.org/10.1016/0031-9201(87)90076-8)
- Moore, J. D., Yu, H., Tang, C.-H., Wang, T., Barbot, S., Peng, D., et al. (2017). Imaging the distribution of transient viscosity after the 2016 Mw 7.1 Kumamoto earthquake. *Science*, *356*(6334), 163–167. <https://doi.org/10.1126/science.aal3422>
- Ohtani, R., McGuire, J. J., & Segall, P. (2010). Network strain filter: A new tool for monitoring and detecting transient deformation signals in GPS arrays[J]. *Journal of Geophysical Research*, *115*(B12), B12418. <https://doi.org/10.1029/2010jb007442>
- Okada, Y. (1985). Surface deformation due to shear and tensile faults in a half-space. *Bulletin of the Seismological Society of America*, *75*(4), 1135–1154. <https://doi.org/10.1785/bssa0750041135>
- Pollitz, F. F., Bürgmann, R., & Banerjee, P. (2006). Post-seismic relaxation following the great 2004 Sumatra-Andaman earthquake on a compressible self-gravitating Earth. *Geophysical Journal International*, *167*(1), 397–420. <https://doi.org/10.1111/j.1365-246x.2006.03018.x>
- Ragon, T., & Simons, M. (2021). Accounting for uncertain 3-D elastic structure in fault slip estimates. *Geophysical Journal International*, *224*(2), 1404–1421. <https://doi.org/10.1093/gji/ggaa526>
- Ragon, T., Sladen, A., & Simons, M. (2018). Accounting for uncertain fault geometry in earthquake source inversions—I: Theory and simplified application. *Geophysical Journal International*, *214*(2), 1174–1190. <https://doi.org/10.1093/gji/ggy187>
- Rolandone, F., Nocquet, J.-M., Mothes, P. A., Jarrin, P., Vallée, M., Cubas, N., et al. (2018). Areas prone to slow slip events impede earthquake rupture propagation and promote afterslip. *Science Advances*, *4*(1), eaao6596. <https://doi.org/10.1126/sciadv.aao6596>
- Scholz, C. H. (1998). Earthquakes and friction laws. *Nature*, *391*(6662), 37–42. <https://doi.org/10.1038/34097>
- Twardzik, C., Vergnolle, M., Sladen, A., & Tsang, L. L. (2021). Very early identification of a bimodal frictional behavior during the post-seismic phase of the 2015 Mw 8.3 Illapel, Chile, earthquake. *Solid Earth Discussions*, 1–24.
- Vajedian, S., Motagh, M., Mousavi, Z., Motaghi, K., Fielding, E., Akbari, B., et al. (2018). Coseismic deformation field of the Mw 7.3 12 November 2017 Sarpol-e Zahab (Iran) earthquake: A decoupling horizon in the northern Zagros mountains inferred from InSAR observations. *Remote Sensing*, *10*(10), 1589. <https://doi.org/10.3390/rs10101589>
- Wallace, L. M., Kaneko, Y., Hreinsdóttir, S., Hamling, I., Peng, Z., Bartlow, N., et al. (2017). Large-scale dynamic triggering of shallow slow slip enhanced by overlying sedimentary wedge. *Nature Geoscience*, *10*(10), 765–770. <https://doi.org/10.1038/ngeo3021>
- Wang, K., & Bürgmann, R. (2020). Probing fault frictional properties during afterslip updip and downdip of the 2017 Mw 7.3 Sarpol-e Zahab earthquake with space geodesy. *Journal of Geophysical Research: Solid Earth*, *125*(11), e2020JB020319. <https://doi.org/10.1029/2020jb020319>
- Wang, K., & Fialko, Y. (2018). Observations and modeling of coseismic and postseismic deformation due to the 2015 Mw 7.8 Gorkha (Nepal) earthquake[J]. *Journal of Geophysical Research: Solid Earth*, *123*(1), 761–779. <https://doi.org/10.1002/2017jb014620>
- Wang, R., Marín, F. L., & Roth, F. (2003). Computation of deformation induced by earthquakes in a multi-layered elastic crust—FORTRAN programs EDGRN/EDCMP. *Computers & Geosciences*, *29*(2), 195–207. [https://doi.org/10.1016/s0098-3004\(02\)00111-5](https://doi.org/10.1016/s0098-3004(02)00111-5)
- Wang, R., Schurr, B., Milkereit, C., Shao, Z., & Jin, M. (2011). An improved automatic scheme for empirical baseline correction of digital strong-motion records. *Bulletin of the Seismological Society of America*, *101*(5), 2029–2044. <https://doi.org/10.1785/0120110039>
- Wei, S., Barbot, S., Graves, R., Lienkaemper, J. J., Wang, T., Hudnut, K., et al. (2015). The 2014 Mw 6.1 south Napa earthquake: A unilateral rupture with shallow asperity and rapid afterslip. *Seismological Research Letters*, *86*(2A), 344–354. <https://doi.org/10.1785/0220140249>
- Williams, S., Bock, Y., & Fang, P. (1998). Integrated satellite interferometry: Tropospheric noise, GPS estimates and implications for interferometric synthetic aperture radar product. *Journal of Geophysical Research*, *103*(B11), 27051–27068. <https://doi.org/10.1029/98jb02794>
- Yue, H., Sun, J., Wang, M., Shen, Z., Li, M., Xue, L., et al. (2021). The 2019 Ridgecrest, California earthquake sequence: Evolution of seismic and aseismic slip on an orthogonal fault system. *Earth and Planetary Science Letters*, *570*, 117066. <https://doi.org/10.1016/j.epsl.2021.117066>
- Yue, H., Zhang, Y., Ge, Z., Wang, T., & Zhao, L. (2020). Resolving rupture processes of great earthquakes: Reviews and perspective from fast response to joint inversion. *Science China Earth Sciences*, *63*(4), 492–511. <https://doi.org/10.1007/s11430-019-9549-1>